Journal of Materials Chemistry C

ROYAL SOCIETY OF CHEMISTRY

PAPER

View Article Online
View Journal | View Issue

Cite this: J. Mater. Chem. C, 2025, 13, 23889

Tuning the excitation-regime-dependent nonlinear optical responses of Cu-doped NiO thin films for harmonic generation and ultrafast photonic applications

Ramseena Thundiyil, [a] P. Poornesh, *[a] Katarzyna Ozga,[b] Jaroslaw Jedryka,[b] Dominique Guichaoua,[c] Said Taboukhat, [c] Saikat Chattopadhyay [d] and Bouchta Sahraoui [c]

Advanced nonlinear optical (NLO) materials with engineered structural and optical characteristics are increasingly vital for meeting modern technological demands due to their multifunctional capabilities. Cu doped NiO thin films were synthesized using spray pyrolysis and investigated for their structural, linear, and nonlinear optical properties. Cu incorporation significantly modified crystallinity, surface morphology, and the formation of defect states, influencing the multifunctional behavior of the films. The third-harmonic generation (THG) efficiency of the films displayed distinct excitation-dependent behavior. The 1 wt% Cu-doped film showed the highest THG efficiency under nanosecond excitation, attributed to enhanced linear and nonlinear interactions facilitated by longer pulse durations, while the 3 wt% Cu-doped film exhibited maximum THG response under picosecond excitation, reflecting the role of electronic structure and ultrafast carrier dynamics in short-pulse regimes. Z-scan analysis revealed that the films exhibit reverse saturable absorption from sequential two-photon processes and a negative nonlinear refractive index arising from thermally induced self-defocusing. The observed enhancement in both THG and Z-scan responses is attributed to the interplay of Cu-induced defect states, modified electronic transitions, and dynamic nonlinear interactions across different temporal excitation regimes. These findings establish Cu-doped NiO thin films as efficient and versatile NLO materials, suitable for applications in optical limiting, laser safety, and integrated photonic devices.

Received 17th September 2025,
Accepted 27th October 2025

DOI: 10.1039/d5tc03464g

rsc.li/materials-c

1. Introduction

The rapid advancement of laser photonics and optoelectronic technologies has intensified the demand for advanced nonlinear optical (NLO) materials, particularly for applications such as all-optical switching, optical limiting, and photonic signal processing. In this context, semiconductor nano-thin films of metal oxides have emerged as highly promising materials due to their compatibility with device architectures and their distinct physical and optical properties.[1,2] Nanoscale engineering offers the ability to tailor material functionalities by designing semiconductor nanomaterials with enhanced or synergistic properties. Integrating different types of nanomaterials allows precise control over their structural, chemical, and optical characteristics, thereby enabling the development of customized materials with superior performance for laser-based and photonic applications.[3]

Among various classes of materials, transition metal oxides (TMOs) have attracted increasing attention in recent years, owing to their unique combination of low electrical resistivity and high optical transparency. Binary metal oxide TMOs are of interest due to their cost-effective synthesis, non-toxic nature, and environmental compatibility, making them ideal candidates for optoelectronic device fabrication. Nickel oxide (NiO) is a p-type semiconductor that possesses a wide bandgap, excellent optical transmittance, and remarkable chemical stability. Recognized as a multifunctional material, NiO finds applications in energy storage, catalysis, protective coatings, supercapacitors, and sensor technologies.[4,5]

To synthesize NiO in various nanostructured forms, such as nanoflowers,[6] nanofibers,[7] and nanocomposites,[8] numerous methods have been explored, including physical vapor deposition,

[a] Department of Physics, Manipal Institute of Technology, Manipal Academy of Higher Education, Manipal, Karnataka 576104, India.
E-mail: poornesh.p@manipal.edu, poorneshp@gmail.com
[b] Faculty of Electrical Engineering, Czestochowa University of Technology, Armii Krajowej 17, PL-42-201 Czestochowa, Poland
[c] Univ Angers, LPHIA, SFR MATRIX, F-49000 Angers, France
[d] Department of Physics, School of Physical and Biological Sciences, Manipal University Jaipur, Rajasthan-303007, India

sputtering, and solution-based techniques like spin coating, dip coating, and spray pyrolysis.[9,10] Among these, spray pyrolysis stands out for its simplicity, scalability, and effectiveness in producing uniform thin films with controllable thickness, high surface-to-volume ratio, and ease of dopant incorporation.

To modify the properties of NiO nanostructures, various synergistic approaches have been reported, including doping, annealing, irradiation, heterojunction formation, and composite fabrication. Among these, doping has been found to significantly influence the nonlinear optical (NLO) properties by altering defect states, bandgap energy, and electronic polarizability. These changes have a profound impact on optical nonlinear behavior, making doped NiO materials highly suitable for enhancing third-order NLO performance.

Among various doping strategies, the incorporation of copper ions (Cu^{2+}) into the NiO matrix has proven particularly effective due to the close match in ionic radii between Cu^{2+} (0.73 Å) and Ni^{2+} (0.69 Å). This similarity enables efficient substitution of Cu^{2+} into the NiO lattice with minimal structural strain, resulting in a stable crystal framework. The substitution induces localized lattice distortions, leading to notable changes in the material's structural and optical properties, key factors that contribute to enhanced third-order nonlinear optical behavior.

Although NiO has been extensively studied for various optical applications, its potential as an NLO material, particularly when doped with copper, remains underexplored. There is a lack of systematic studies on the third-order NLO response of Cu-doped NiO thin films, especially those synthesized *via* scalable spray pyrolysis methods. Furthermore, the influence of laser excitation, such as nanosecond laser, picosecond laser, and continuous wave laser, plays a crucial role in determining the nonlinear behavior of materials. Therefore, investigating the NLO response of Cu-doped NiO under different laser regimes is essential for advancing its application in photonic technologies.

In this study, nano-thin films of pristine and Cu-doped NiO were synthesized using the spray pyrolysis technique. The focus was on optimizing the copper doping concentration and analyzing its effects on the films' structural, linear optical, and third-order nonlinear optical properties. A systematic investigation was conducted to understand how Cu doping influences morphology, crystallinity, bandgap, and nonlinear response. To evaluate third-order NLO behavior, Z-scan measurements were performed using a continuous-CW laser at 633 nm, and third-harmonic generation THG studies were conducted under different pulsed laser regimes. These measurements provide both qualitative and quantitative insights into the NLO performance of Cu-doped NiO as a function of doping concentration.

2. Experimental details

2.1. Preparation of Cu doped NiO (Cu–NiO) thin films

Thin films of Cu-doped NiO (Cu–NiO) were developed through a chemical route employing the spray-pyrolysis technique. Nickel acetate tetrahydrate and copper(II) chloride dihydrate were used as the host and dopant precursor salts, respectively. Deionized water served as the solvent for solution preparation. To ensure homogeneity, both solutions were magnetically stirred for one hour. Subsequently, the dopant solution was mixed with the host solution in concentrations of 1, 3, 5, 7, and 10 wt%.

Soda-lime glass slides were used as substrates to deposit Cu–NiO thin films. The cleaning of the glass substrate was carried out for a total of 30 minutes: 10 minutes in deionized water, 10 minutes in acetone, and the remaining 10 minutes in isopropanol solutions, all of which were ultrasonic bath cleaning, respectively. Then the glass substrate is dried with the hot air dryer.

Afterward, the prepared dopant solutions with the required volume were filled in the spray syringe and sprayed on the 450 °C preheated substrate using the spray pyrolysis technique. The distance between the spray nozzle and the substrate was maintained at 12 cm during deposition. The compressed air maintenance was at 0.3 bar, and the flow rate was kept at 2 ml min^{-1}. Compressed air was used to generate aerosols (fine droplets) of the spray solution as it exited the nozzle. Upon reaching the heated substrate, these aerosols underwent thermal decomposition, resulting in the formation of thin films on the substrate. The volatile by-products were removed through exhaust. Using a profilometer, the thickness was determined to be approximately 300 nm for the obtained Cu–NiO thin films. The experimental procedure of this study was depicted in the schematic representation presented in Fig. 1.

2.2. Details of material characterization

The properties of the prepared Cu–NiO thin films were studied using various characterization techniques. The crystallographic structure, phase identification, and crystallinity were analyzed using an X-ray diffractometer (Rigaku SmartLab). XRD patterns were recorded in the 2θ range of 30° to 90° with a scanning speed of 1° min^{-1}, using Cu Kα radiation (λ = 1.5406 Å). Raman analysis was employed to investigate the phase purity and vibrational characteristics of the films. The spectra were collected using a HORIBA Scientific Raman spectrometer equipped with LabSpec 6 software. A 532 nm laser with an edge filter was used for excitation, and a neutral density (ND) filter of 10% was applied to control the laser power. The grating used was 600 grooves per mm (centered at 500 nm), and the spectra were acquired with an accumulation of 8 scans to improve the signal-to-noise ratio. The linear optical parameters, such as absorbance and energy bandgap (derived from the absorbance data), were determined using a UV-visible spectrophotometer (Shimadzu, UV-1900i) over the wavelength range of 190 to 1100 nm. The presence of defects in the prepared thin films was analyzed using photoluminescence (PL) spectroscopy. PL measurements were performed with a JASCO FP-8500 spectrofluorometer, using a xenon lamp as the excitation source. The excitation wavelength was fixed at 300 nm for all samples, and the emission spectra were recorded at room temperature. The surface topographical variations of

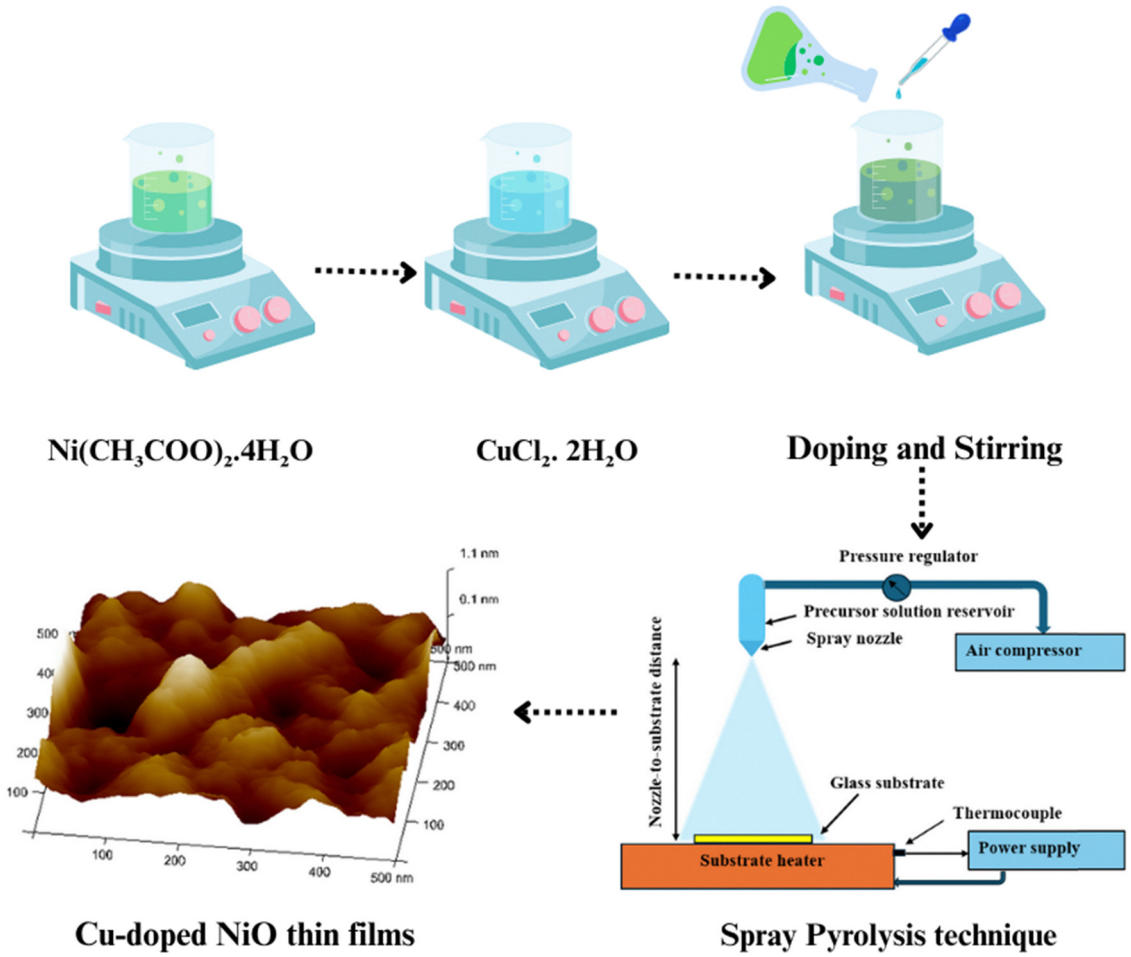

Fig. 1 Schematic of the experimental procedure for preparing Cu–NiO thin films.

all samples were analyzed using atomic force microscopy (AFM, Innova SPM) operated in non-contact (tapping) mode. The elemental composition and chemical states of the thin films were analyzed by X-ray photoelectron spectroscopy (XPS). The spectra were acquired using a Kratos AXIS ULTRA spectrometer equipped with a monochromatic Al Kα radiation source ($h\nu$ = 1486.6 eV), operated at 14 kV.

2.3. Nonlinear optical measurements

Third harmonic generation (THG) measurements were conducted to investigate the nonlinear optical response of the prepared thin films and to assess their ability to produce third harmonic signals when exposed to a fundamental laser frequency. Two different methods were employed for the THG measurements. In the first method, the laser fluence was varied under nanosecond excitation. In the second method, the sample rotation angle was varied under picosecond excitation, following the Maker fringes technique.

2.3.1. THG measurement under nanosecond excitation (fluence-dependent study). THG analysis was performed with a photoinduced nonlinear optical setup equipped with a Nd:YAG pulsed laser operating at a wavelength of 1064 nm. The laser produced pulses with a duration of 8 nanoseconds at a repetition rate of 10 Hz, with a beam diameter of about 8 mm. To adjust the incident laser fluence, a Glan polarizer was employed, ensuring operation below the laser damage threshold of 4 GW cm^{-2}. The fundamental laser beam was then divided into two coherent paths using the semi-transparent mirrors. One of the beams was directed towards a monitoring unit to control and stabilize the fundamental laser intensity, while the other was used to probe the third harmonic signal generated by the sample. The THG signal was separated from the fundamental beam using an interference filter centered at 355 nm, and its spectral characteristics were analyzed using a DFS8 spectrometer equipped with diffraction gratings, offering a spectral resolution of approximately 0.2 nm. The intensity of the fundamental beam was measured using a silicon photodetector, whereas the THG signal was detected by a highly sensitive Hamamatsu photomultiplier. Both signals were simultaneously recorded using a Tektronix MSO 3054 oscilloscope with a sampling rate of 2.5 giga samples per second, allowing precise time-resolved acquisition. The entire experimental setup was enclosed in a protective housing to eliminate external light interference and ensure accurate signal detection. The schematic diagram of the experimental setup is shown in Fig. S1.

2.3.2. THG measurement under picosecond excitation (Maker fringes technique). THG measurements were performed using the Maker fringe technique (Fig. S2). The setup employed a pulsed picosecond YVO_4:Nd laser (EKSPLA PL2250) with a wavelength of 1064 nm, 30 ps pulse duration, 95 mJ energy, and 10 Hz repetition rate as the light source. The laser beam first encounters a beam splitter; the reflected part is directed to a photodiode for pulse monitoring, while the transmitted beam passes through a polarizer and half-wave plate to adjust its polarization and energy. The polarized beam is then focused onto the sample using a focusing lens. The sample, in the form of a thin layer, is mounted on a motorized rotation stage allowing precise angular adjustments from -30° to $+30^\circ$ in 0.5° steps. The rotation axis is aligned near the lens's focal point to maximize the incident beam energy at all angles. After interacting with the sample, the beam passes through a KG3 filter to block the fundamental wavelength, followed by a 355 nm interference filter to isolate the third harmonic signal. The THG signal is then detected by a photomultiplier tube (PMT). The photodiode and PMT were interfaced with a controller, oscilloscope, and computer to enable synchronized operation, signal recording, and subsequent data processing. Finally, the angular dependence of the THG signal (Maker fringes) is recorded by rotating the sample.

2.3.3. Z-scan technique. A helium–neon (He–Ne) laser (THORLABS INC, HRP350-EC-1; Research Electro-Optics, Boulder, Colorado) with an output power of 35.0 mW at a wavelength of 633 nm was used as the light source, operating at a voltage of 230 V. A neutral density filter (FILTER Wheel, HOLMARC) was employed to adjust the laser intensity, and an input power of 20 mW was selected to irradiate the sample.

In the experimental setup, a converging lens of 5 cm focal length was employed to concentrate the laser beam onto the sample surface. The spot size at the focal point was measured to be 35.1 μm, corresponding to an on-axis peak intensity of 10.3 MW m^{-2} at the beam waist.

The transmitted beam power was measured using an optical power meter (Thorlabs S121C). A photodetector equipped with an aperture (MSSID 12, HOLMARC) of area $S = 0.7$ was placed in front of the detector to allow only the central portion of the transmitted beam to be detected. A schematic diagram of the experimental setup for the Z-scan measurements is shown in Fig. S3.

3. Results and discussion

3.1. XRD analysis

XRD measurements were conducted to assess the structural alterations induced by Cu incorporation in NiO thin films. The diffraction patterns provide insights into crystallite size, strain, and phase purity. The glancing XRD plot of Cu–NiO thin film is given in Fig. 2a. All the diffraction peaks are characteristic of the cubic crystal structure of NiO with space group $Fm\bar{3}m$ (JCPDS no. 01-078-0643). The atomic arrangement during crystallization follows a face-centered cubic (FCC) lattice, where Ni^{2+} ions occupy the FCC positions and O^{2-} ions fill the octahedral interstitial sites. Each Ni^{2+} ion is octahedrally coordinated by six O^{2-} ions, and *vice versa*, forming a stable rock-salt structure. Other than NiO characteristic peaks, no secondary phase of nickel and copper was detected, confirming the phase purity and the structural stability of the thin films. The undoped NiO thin film exhibits dominant reflections along the (200) plane, indicating the preferred orientation in that direction. Upon 3% Cu doping, the preferred orientation shifts toward the (111) plane. This reorientation is primarily attributed to compositional changes and lattice distortion induced by the incorporation of Cu^{2+} ions into the NiO lattice, which disrupts the regular crystallographic growth pattern.[11]

A noticeable enhancement in the (200) diffraction peak was found at 1 wt% Cu doping, indicating improved crystallinity at lower doping levels. This enhancement may be attributed to reduced lattice strain and better structural ordering. However,

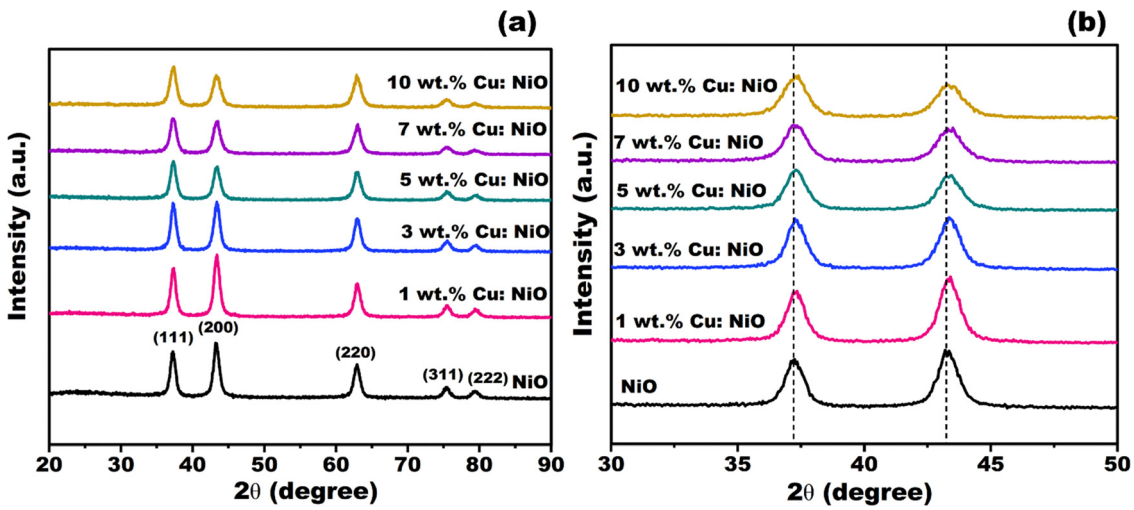

Fig. 2 (a) XRD spectra of Cu–NiO thin films; (b) enlarged view of the (111) and (200) peak shifts.

at higher Cu concentrations, a decrease in peak intensity was noted, likely due to increased lattice distortion and the formation of surface impurities as Cu^{2+} ions substitute Ni^{2+} ions in the NiO matrix. Along with the intensity variations, broadening of the diffraction peaks was also observed, which became more pronounced with increasing Cu doping. This peak broadening is attributed to lattice distortion resulting from the substitution of Cu atoms into the NiO lattice.

To quantify the degree of growth orientation in samples, we employed the texture coefficient (TC) equation, defined as follows:

$$TC_{(hkl)} = \frac{\frac{I_{meas(hkl)}}{I_{0(hkl)}}}{\frac{1}{N}\sum\left(\frac{I_{(hkl)}}{I_{0(hkl)}}\right)} \quad (1)$$

In this equation, $I_{meas(hkl)}$ denotes the measured intensity of the (*hkl*) plane in the XRD pattern, while $I_{0(hkl)}$ refers to the corresponding standard intensity from the JCPDS database. *N* represents the total number of diffraction peaks included. TC offers insight into the preferred crystallographic orientation of crystallites within the film. A TC value of 1 denotes random orientation, while values greater than 1 indicate preferential growth along a specific plane. In this study, TC values were calculated for both (111) and (200) planes to assess orientation tendencies, as summarized in Table 1. The TC for the (111) plane exceeded 1, suggesting a dominant growth orientation along this plane. For the (200) plane, the TC initially increased by 1 wt% Cu doping but subsequently dropped below 1 at higher concentrations. This trend indicates that the crystallite growth direction changes from the (200) plane in the pristine film to the (111) plane in films with higher Cu content (5–10 wt%), reflecting a reorientation of crystallite growth with increasing dopant concentration.

Although Cu^{2+} has a slightly larger ionic radius than Ni^{2+}, a slight reduction in the lattice parameter was observed upon Cu doping, decreasing from 4.178 Å (pristine) to 4.173–4.175 Å. This slight contraction is likely due to local lattice distortions, oxygen vacancies, and strain effects introduced by dopant incorporation, which override the expected lattice expansion based solely on ionic size. The diffraction peak exhibited a non-monotonous shift with increasing Cu doping (Fig. 2b). Initially, the peak shifted toward higher 2θ values (from 37.24° to 37.31° at 3 wt% Cu), indicating a slight lattice contraction due to Cu^{2+} substitution and possible oxygen vacancy formation. Additionally, the presence of nickel vacancies can lead to the oxidation of Ni^{2+} to smaller Ni^{3+} ions, which further contributes to lattice contraction and thus a shift in the XRD peak toward higher 2θ values.[12] However, with further doping (5–10 wt%), the peak gradually shifted back toward lower angles, suggesting strain relaxation, increased defect concentration, or dopant-induced lattice disorder, which counteract the initial contraction. Javadian *et al.*[13] also reported a similar non-monotonous shift in the XRD peak position with increasing Cu doping. They explained that at lower Cu concentrations, Cu^{3+} ions replace Ni^{3+} ions, causing lattice contraction and a shift to higher 2θ values. At higher Cu concentrations, Cu^{2+} ions substitute for Ni^{2+}, leading to lattice expansion and a shift to lower 2θ values.

The crystallite size of the Cu–NiO thin films was calculated from the size-strain plot,[14] given by,

$$(d_{hkl}\beta_{hkl}\cos\theta)^2 = \frac{k\lambda}{D}(d_{hkl}{}^2\beta_{hkl}\cos\theta) + \frac{\varepsilon^2}{4} \quad (2)$$

where *k* is the constant and ε refers to the micro-strain induced within the crystal lattice. The size-strain plots are presented in Fig. S4. The crystallite size increased from 8.70 nm (pristine) to 8.82 nm at 1 wt% Cu doping, then decreased to 8.52–7.12 nm with higher doping concentrations. The slight increase at 1% is due to the effective substitution of Cu^{2+} into Ni^{2+} sites, which stabilizes the lattice and promotes crystallite growth. However, at higher doping levels (3–10%), increased Cu^{2+} substitution, with its slightly larger ionic radius (0.72 Å *vs.* 0.69 Å for Ni^{2+}), induces lattice distortion. Additionally, enhanced nucleation rates and the approach toward the solubility limit of Cu^{2+} contribute to reduced crystallite size. The reduction in crystallite size at higher doping levels is also influenced by increased lattice strain and defect accumulation induced by Cu^{2+}.[15] Moreover, the reduction in crystallite size can also be attributed to the Zener pinning effect induced by Cu doping, where Cu atoms act as obstacles to grain boundary movement, thereby suppressing grain growth.[13,16] The overall reduction in average crystallite size as Cu content increases is attributed to strain resulting from ionic mismatch and defect-assisted doping. These structural modifications, particularly the induced strain and reduced crystallite size, are expected to influence the optical and nonlinear responses, as discussed in subsequent sections.

Additional structural parameters, including interplanar spacing (*d*), lattice constant (*a*), lattice strain (ε), dislocation density (δ), and the number of crystallites per unit volume (*N*), were calculated using standard equations, and

Table 1 Structural parameters extracted from the XRD pattern of Cu–NiO thin films

Cu dopant concentration (wt%)	$d_{(111)}$ (Å)	*a* (Å)	$\beta_{(111)}$ (deg.)	Crystallite size (nm)	Dislocation density ($\times10^{16}$ m^{-2})	Strain ($\times10^{-2}$)	No. of crystallites ($\times10^{17}$ m^{-3})	TC(111)	TC(200)
0	2.412	4.177	0.981	8.70	1.32	1.27	4.56	0.98	0.82
1	2.409	4.173	0.969	8.82	1.29	1.25	4.37	0.97	0.86
3	2.408	4.173	0.995	8.52	1.38	1.29	4.84	0.96	0.70
5	2.409	4.173	1.051	7.97	1.57	1.36	5.92	1.13	0.67
7	2.410	4.174	1.132	7.52	1.77	1.46	7.05	1.14	0.70
10	2.411	4.175	1.187	7.12	1.97	1.54	8.30	1.12	0.62

the corresponding values are presented in Table 1. The formulas used are as follows:

$$d = \frac{\lambda}{2\sin\theta} \quad (3)$$

$$a = d\sqrt{h^2 + k^2 + l^2} \quad (4)$$

$$\varepsilon = \frac{\beta}{4\tan\theta} \quad (5)$$

$$\delta = \frac{1}{D^2} \quad (6)$$

$$N = \frac{t}{D^3} \quad (7)$$

where t refers to the thickness of the prepared thin films. At 1 wt% doping, both strain and dislocation density decrease, indicating fewer lattice defects and more stable grain boundaries. In contrast, higher doping concentrations result in increased strain and dislocation density due to enhanced defect formation within the NiO lattice.[17]

3.2. Raman analysis

Raman analysis was conducted to examine the vibrational characteristics, structural arrangement, phase distribution, and defect features of the samples. Typically, cubic phase NiO exhibits characteristic peaks corresponding to first- and second-order longitudinal optical (LO) and transverse optical (TO) phonon modes. These include the 1TO, 1LO, 2TO, 2LO, and combination modes such as LO + TO. Among these, the LO mode is attributed to the stretching vibrations of the Ni–O bond. These Raman-active LO modes are generally absent or very weak in stoichiometric NiO films due to their centrosymmetric crystal structure, which forbids first-order Raman scattering. However, in the present study, the appearance of LO modes indicates the non-stoichiometric nature of the prepared films. This suggests the presence of Ni^{3+} ions and associated defect states such as oxygen vacancies.[18] The activation of the LO mode is often attributed to the breakdown of inversion symmetry (parity selection rule) in the Ni–O lattice, likely due to defect-induced lattice distortion or disorder. The intensity peak of TO, TO + LO, and 2LO is very small compared to the LO mode; this is associated with the smaller crystallite size of the thin film material. The Raman analysis confirmed the absence of the secondary peak; the result is in line with the XRD results.

Fig. 3 presents the Raman spectra of the Cu-doped NiO thin film. To accurately determine the peak positions and full width at half maximum, the observed Raman modes were deconvoluted using Gaussian fitting. The Raman spectrum of the NiO thin film displays a broad band in the range of 250–700 cm^{-1}, which arises from overlapping phonon modes. Specifically, peaks at 384.85 cm^{-1} and 503.24 cm^{-1} are attributed to the 1TO and 1LO modes of Ni–O vibrations, respectively. Additionally, weak bands observed at 989.95 cm^{-1} and 1101.55 cm^{-1} correspond to the LO + TO combination, as well as 2LO stretching mode of NiO. The peak positions and Raman FWHM values of the Cu-doped NiO films are summarized in Table S1.

A significant enhancement in the intensity of the first-order Raman peaks is observed upon Cu doping when compared to pure NiO. This suggests an increase in non-stoichiometry

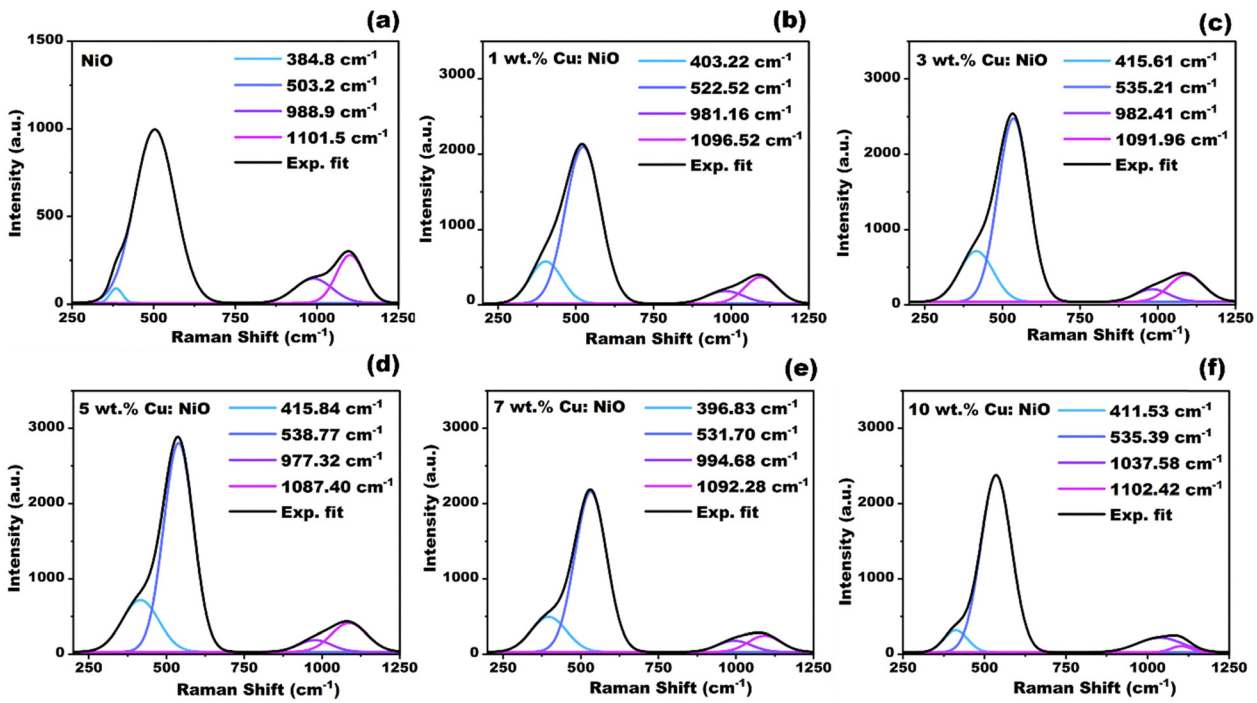

Fig. 3 Raman spectra of Cu-doped NiO films showing characteristic peak positions for different Cu doping concentrations: (a) 0 wt%, (b) 1 wt%, (c) 3 wt%, (d) 5 wt%, (e) 7 wt%, and (f) 10 wt%.

resulting from Cu incorporation, which is indicative of a higher concentration of Ni and interstitial oxygen vacancies in the crystal structure. The increased efficiency of the first-order Raman modes confirms the rise in defect density in the Cu-doped samples.

However, the intensity does not vary monotonically with Cu content. The highest Raman intensity is observed for the 5 wt% Cu-doped sample, followed by 3 wt%, 10 wt%, 7 wt%, and 1 wt%, respectively. This trend implies that the maximum concentration of nickel and oxygen-related vacancies occurs at 5 wt% Cu doping. The LO and TO phonon modes, which are sensitive to lattice defects, show increased intensity with doping, further supporting the presence of enhanced defect concentrations, particularly nickel vacancies.

As illustrated in Fig. S5(a) and (b), a noticeable broadening of the Raman peaks is observed after Cu doping. This broadening, especially of the 1TO mode, is primarily attributed to increased defect concentration, lattice disorder, and phonon confinement effects due to reduced crystallite size. These factors disrupt the coherence and lifetime of phonon vibrations, leading to wider spectral features.

In addition, Cu doping causes shifts in the Raman bands (shown in Fig. S5(c)). These spectral shifts are primarily due to the replacement of Ni^{2+} by Cu^{2+} within the NiO lattice, which induces lattice defects, dislocations, and compressive strain. Specifically, the 1TO and 1LO modes shift to higher wavenumbers, which can be attributed to strain and increased defect densities introduced by Cu incorporation.

3.3. UV-Visible analysis

The absorbance and energy bandgap were recorded by a UV-vis spectrophotometer, and it is given in Fig. 4. Based on the absorbance graph, the UV region shows the highest absorbance, while the near-IR region exhibits the lowest. The pronounced absorption in the UV region originates mainly from electronic transitions between the O(2p) states in the valence band and the Ni(3d) states in the conduction band of NiO. These transitions involve the absorption of photon energy, resulting in the prominent spectral features observed in this region.[19] The absorbance increases with the doping concentration; this is associated with the increased copper content, which introduces more imperfections and enhances light absorption in the ultraviolet range. The substitution of Ni^{2+} ions by Cu^{2+} creates additional defect states and Ni^{2+} vacancies, increasing the number of absorbing centers.[20] This leads to stronger light–matter interaction and, consequently, higher absorption intensity. It should be mentioned that doping causes the absorption edge to redshift, which validates the energy bandgap's contraction.

The energy band gap was calculated using Tauc's relation, shown in Fig. 5. Observed a decrease in the band gap for Cu-doped NiO films. The band gap values were 3.59, 3.56, 3.55, 3.49, 3.44, and 3.27 eV for pure NiO and Cu-doped NiO with 1%, 3%, 5%, 7%, and 10% Cu concentrations, respectively. The variation in the energy band gap with increasing Cu concentration is schematically illustrated in Fig. S6. A clear reduction

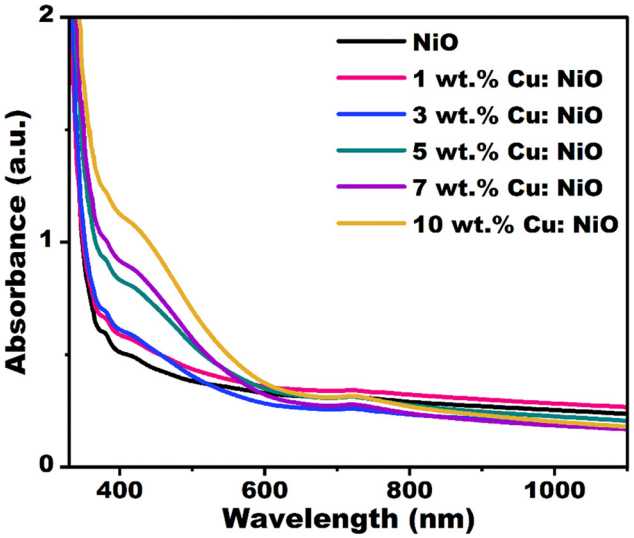

Fig. 4 Absorbance spectra of Cu–NiO thin films.

in band gap energy is observed as the Cu doping level increases. This narrowing is primarily attributed to the introduction of defect states and localized impurity levels within the band gap, arising from the substitution of Cu^{2+} ions into the NiO lattice. These impurity states modify the electronic structure through sp–d exchange interactions between the Cu 3d electrons and the conduction band, as well as d–d exchange interactions between the localized 3d electrons of Cu^{2+} and Ni^{2+}.

Additionally, the incorporation of Cu introduces Cu 3d states near the Fermi level, contributing to the broadening of the valence band and further narrowing the band gap.[21] The enhanced hybridization between Ni 3d and O 2p orbitals due to Cu substitution also plays a role in reducing the band gap. Furthermore, compressive stress induced by the smaller Cu^{2+} ions within the NiO lattice can affect the crystal field, contributing to this energy band gap shrinkage.[16] Collectively, these factors result in a systematic and progressive decrease in the band gap with increasing Cu doping concentration.

3.4. PL analysis

Photoluminescence (PL) spectroscopy is a sensitive tool to probe optical transitions and defect states in semiconductors. In NiO nanostructures, PL emission arises primarily from near-band-edge recombination and deep-level emissions (DLE) associated with intrinsic defects, including nickel and oxygen nonstoichiometric defects. The Gaussian-fitted PL spectra of Cu–NiO thin films with an excitation wavelength of 300 nm at room temperature and given in Fig. 6. The PL spectra exhibit multiple emission bands ranging from the UV to the visible region. A dominant UV emission near 398–400 corresponds to near-band-edge (NBE) emission, while the visible emissions, violet (~422–425 nm), blue (~435–470 nm), orange (~571 nm), and yellow (~611–614 nm), are attributed to defect-related transitions.

Each emission is assigned to a specific defect-related transition. For instance, in NiO thin films, the UV emission

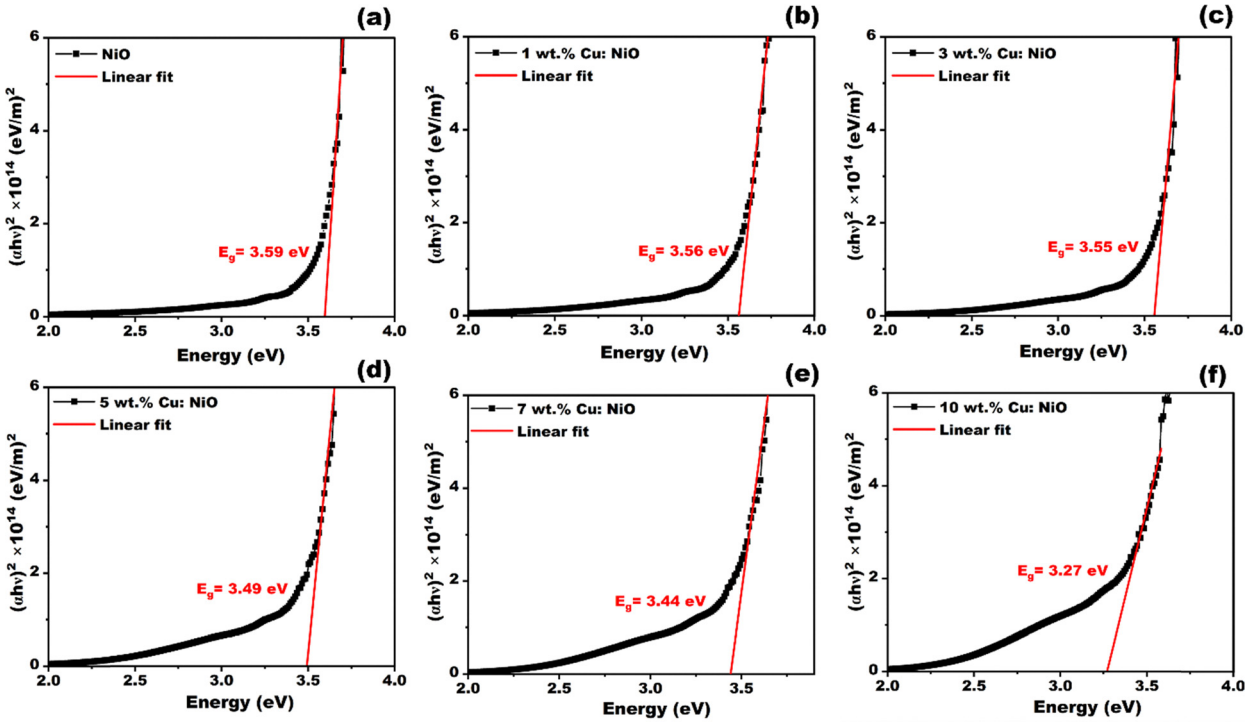

Fig. 5 Tauc's plots of NiO thin films with varying Cu doping: (a) 0 wt%, (b) 1 wt%, (c) 3 wt%, (d) 5 wt%, (e) 7 wt%, and (f) 10 wt% showing band gap variation.

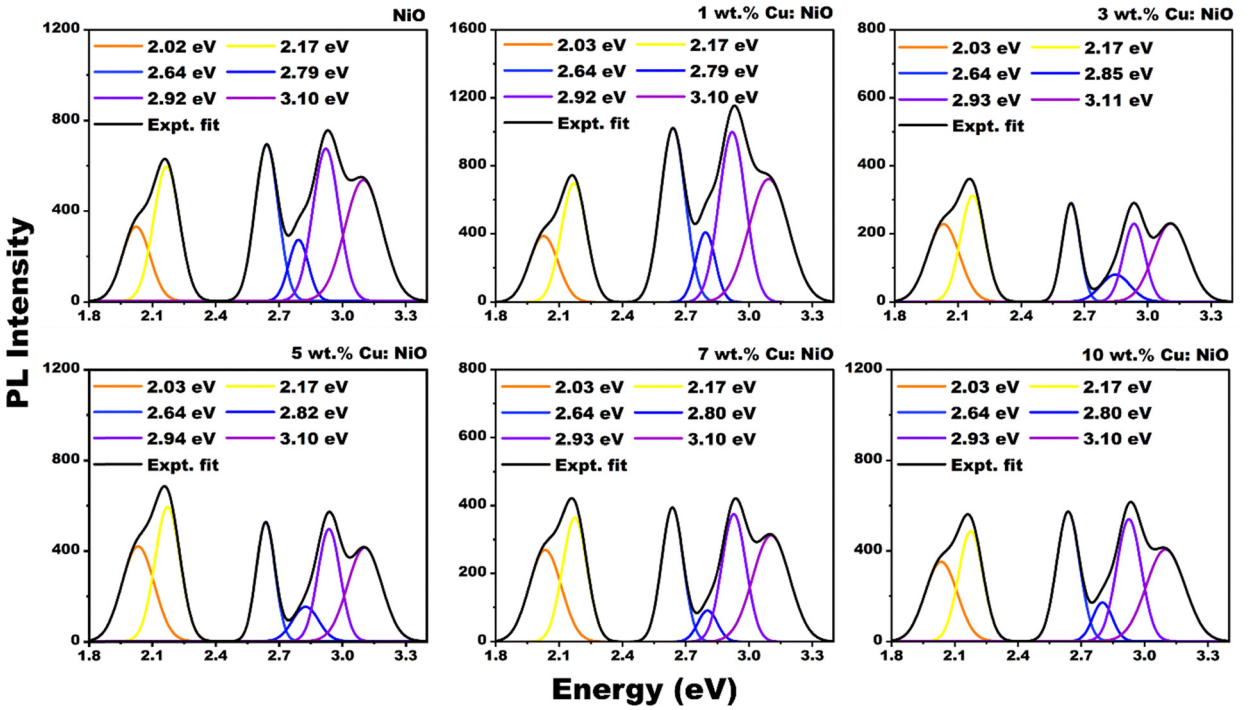

Fig. 6 Deconvoluted PL spectra of Cu–NiO thin films.

(at 3.10 eV) is associated with exciton recombination near the band edge, whereas other deep-level emissions occur in the visible region. The DLE consists of interstitials and vacancies of nickel and oxygen, which introduce defect states within the forbidden band gap. The excited electron de-excitation from nickel interstitial to valence band state corresponds to the PL peak position at 2.92 eV. The peaks at 2.79 and 2.64 eV are related to the blue emission and are associated with nickel

vacancy levels to the VB.[22] In particular, the 2.64 eV emission arises from the radiative recombination of holes in the valence band with electrons trapped in the doubly ionized nickel vacancy level.[23] The emissions at 2.17 and 2.02 eV arise from oxygen-related defects in NiO. Specifically, at 2.17 eV originates from the recombination of electrons from shallow donor states (or the CB) to deep oxygen vacancy levels, which act as hole traps within the band gap. The 2.02 eV emission is attributed to electron transitions from the conduction band to deep interstitial oxygen levels (O_i), which act as electron traps located above the valence band.[24] The PL peak positions and the corresponding broadening related to defect states in Cu–NiO thin films are summarized in Table S2. A simplified band diagram illustrates transitions involving CB, VB, and defect states (V_{Ni}, V_O, Ni_i, O_i), explaining the origin of various emission bands observed and shown in Fig. 7.

The PL intensity shows variation with Cu doping in the NiO matrix. A significant increase is observed at 1 wt% Cu doping compared to the pristine sample, indicating an increase in nickel and oxygen vacancies and interstitials that enhance radiative recombination. However, at higher doping levels, a non-monotonous decline in PL intensity is observed, with the 3 wt% sample exhibiting the lowest emission. This drop is primarily due to the increased formation of non-radiative recombination centers, such as point defects, dislocations, and structural imperfections introduced by excess Cu, leading to PL quenching. Cu^{2+} doping introduces defect states in the NiO lattice that act as trapping sites for excited electrons, promoting non-radiative pathways and suppressing radiative recombination. As the dopant concentration increases, these defect-induced quenching effects become more prominent.[24]

Notably, significant changes in the PL emission peak structure were observed from 3 wt% Cu doping onwards. In the pristine and 1 wt% samples, nickel interstitial-related emissions were the most prominent. However, at 3, 5, and 7 wt% Cu concentrations, the PL intensity associated with oxygen vacancy-related emissions became stronger than those related to nickel interstitials. This indicates that the 3, 5, and 7 wt% samples exhibit distinct emission features dominated by oxygen vacancy defects, which are more pronounced at these doping levels. The intensity of emissions attributed to nickel interstitials was highest for the 1 wt% sample, followed in decreasing order by the 0%, 10%, 5%, 7%, and 3 wt% samples, suggesting that lower Cu content favors the formation of nickel interstitial defects. In contrast, oxygen vacancy-related emissions were most intense in the 1 wt% sample, followed by 5%, 0%, 10%, 7%, and 3 wt%, indicating that Cu doping also facilitates the generation of oxygen vacancies, though their prominence varies non-linearly with doping concentration. While these defect-related emissions are evident, they are insufficient to counteract the increasing non-radiative recombination pathways at higher doping concentrations, which ultimately suppress PL intensity. This quenching behavior is further supported by GAXRD analysis, which shows increased dislocation density, and by the observed broadening of PL peaks, both confirming enhanced non-radiative recombination due to defect accumulation.

No significant shift is observed in the PL peak positions with Cu doping. Minor shifts are common and can be attributed to strain or stress in the lattice. A non-monotonous variation in PL peak broadening is observed with Cu doping. Gradual broadening is generally associated with oxygen interstitials by doping, except at 7 wt%, where this trend deviates. In contrast, oxygen vacancies and nickel interstitials exhibit irregular effects on the broadening. The overall PL broadening is attributed to increased defect densities, particularly oxygen interstitials and nickel vacancies, which introduce multiple recombination pathways, resulting in the observed non-monotonous behavior.

3.5. XPS analysis

The elemental composition, oxidation states, and chemical environment of the prepared thin films were analyzed using X-ray photoelectron spectroscopy (XPS). As shown in Fig. 8a, the

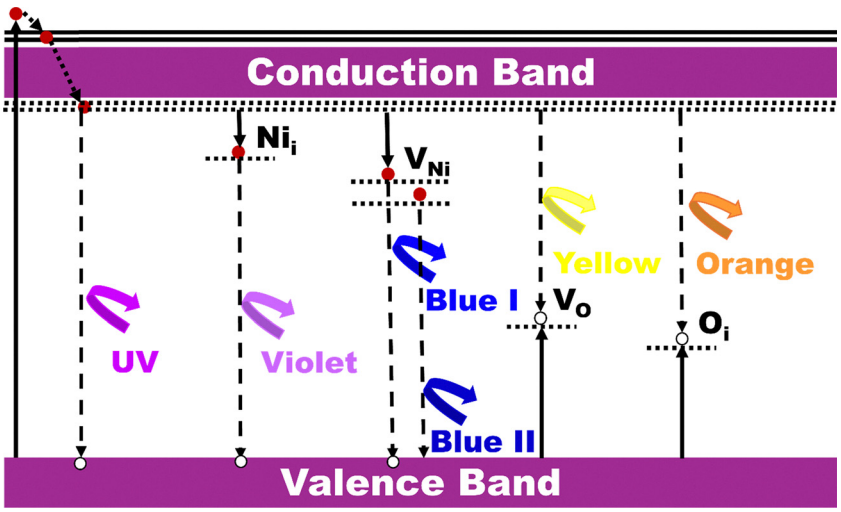

Fig. 7 Simplified band diagram showing PL transitions from CB and defect states to VB, explaining the origin of observed emission peaks.

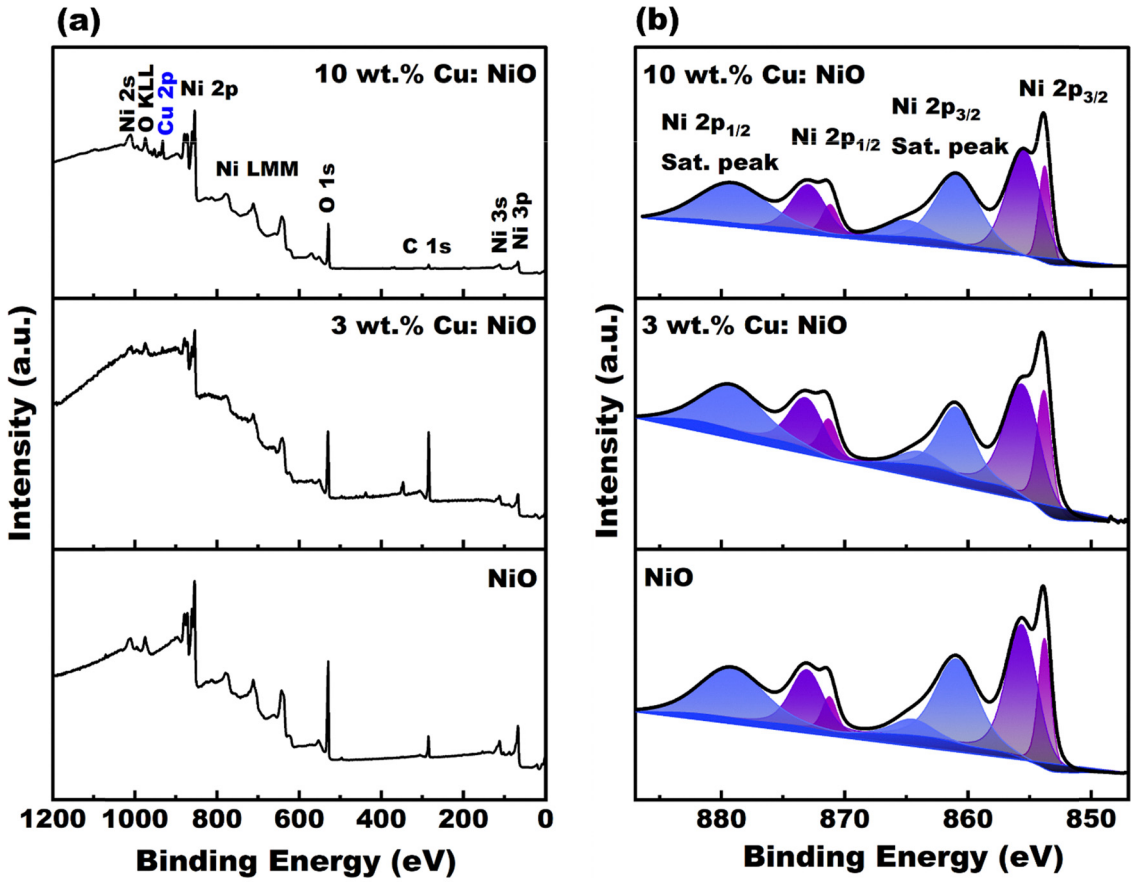

Fig. 8 XPS spectra of NiO, 3 wt%, and 10 wt% Cu–NiO thin films: (a) wide survey scan, and (b) Ni core-level spectra.

wide-scan XPS spectra of the NiO, 3 wt%, and 10 wt% Cu–NiO thin films reveal signals corresponding to Ni, O, C, and Cu elements. The pristine NiO film exhibits characteristic Ni 2p and O 1s peaks, while additional Cu 2p peaks appear in the doped samples, confirming the successful incorporation of Cu into the NiO lattice. The intensity of Cu-related peaks increases with doping concentration, further supporting the progressive substitution of Cu ions in the NiO matrix. Core-level spectra for Ni 2p, Cu 2p, O 1s, and C 1s were clearly identified, along with minor peaks corresponding to Ni 2s, Ni 3s, O KLL, and Ni LMM Auger transitions. The absence of any foreign elements indicates the chemical purity of the films. Binding energies were calibrated using the C 1s peak at 284.8 eV to correct for surface charging effects. The core-level spectra were deconvoluted using the Shirley background and analyzed with CASA XPS software. A Lorentzian–Gaussian (LF) fitting function was applied to resolve different oxidation states and defect-related features.

3.5.1. Ni core level spectra. Fig. 8b shows the deconvoluted Ni 2p spectra, consisting of two main peaks, Ni $2p_{3/2}$ and Ni $2p_{1/2}$, which represent the spin–orbit doublets of the Ni core-level spectra. In the pristine NiO sample, the Ni $2p_{3/2}$ peaks appear at 853.79 and 855.62 eV (Ni^{2+} and Ni^{3+}, respectively) with satellites at 860.89 and 864.53 eV, while the Ni $2p_{1/2}$ peaks are located at 871.24 and 873.06 eV with a satellite at 879.15 eV. The binding energies of Ni $2p_{3/2}$ and Ni $2p_{1/2}$ are 853.82 and 871.29 eV for the 3 wt% Cu–NiO, and 853.77 and 871.18 eV for the 10 wt% Cu–NiO, which are in good agreement with reported values.[25,26] The spin–orbit splitting is 17.47 and 17.41 eV for the 3 and 10 wt% samples, respectively.

In the Ni $2p_{3/2}$ region, peaks at 853.82 and 855.57 eV (3 wt%) and 853.77 and 855.45 eV (10 wt%) correspond to Ni^{2+} and Ni^{3+} states, respectively, with their shake-up satellites appearing at higher binding energies (860.85–860.94 eV and 863.99–865.04 eV).[27,28] Similarly, the Ni $2p_{1/2}$ region displays peaks at 871.29 and 873.12 eV for the 3 wt% film and 871.18 and 872.95 eV for the 10 wt% film, attributed to Ni^{2+} and Ni^{3+} states. A satellite feature at ~879.09–879.12 eV is associated with Ni^{2+}.

The coexistence of Ni^{2+} and Ni^{3+} oxidation states suggests the presence of both ideal and defect-rich NiO phases, with Ni^{3+} commonly associated with nickel vacancies. The satellite peaks originate from enhanced Ni 3d–O 2p hybridization and d–d electronic transitions. Furthermore, a slight shift in the binding energies compared to the pristine sample is observed, which can be attributed to the incorporation of Cu dopant atoms. The substitutional incorporation of Cu modifies the local chemical environment of Ni, inducing lattice distortions and defects that influence the Ni 2p binding energies.

3.5.2. Core level spectra. The O 1s core-level spectrum exhibits an asymmetric profile with multiple overlapping

components, as shown in Fig. 9a. The main peak, centered at 529.29 eV (NiO), 529.71 eV (3 wt%), and 529.39 eV (10 wt%), is attributed to O^{2-} ions in metal–oxygen bonds, where oxygen is coordinated with Ni^{2+} ions in the lattice (denoted as lattice oxygen, O_L).[29,30] The slight shifts in binding energy relative to pristine NiO indicate the influence of Cu doping.

In addition, a peak at 531.16 eV (pristine), 531.47 eV (3 wt%), and 531.28 eV (10 wt%) corresponds to oxygen vacancies (denoted as O_V), confirming the presence of oxygen defect states within the films.[25] The peak observed at 532.66 eV for NiO is attributed to adsorbed molecular water.[26,29] The enhanced area ratio of the oxygen vacancy peak in the doped thin films compared to the pristine sample (41.7%) indicates an increased concentration of O_V defects. Notably, the 3 wt% Cu–NiO thin film exhibits the highest O_V area ratio of 51%, highlighting a significant enrichment of oxygen vacancy defects relative to pristine NiO.

The deconvoluted binding energies and corresponding FWHM values of Ni 2p, Cu 2p, and O 1s core levels for the NiO, 3 wt%, and 10 wt% Cu–NiO thin films are summarized in Table S3.

3.5.3. Cu core level spectra. Fig. 9b shows the deconvoluted Cu 2p spectra of the 3 and 10 wt% Cu–NiO thin films, revealing distinct main and satellite peaks. The Cu 2p core-level spectra consist of two primary peaks corresponding to Cu $2p_{3/2}$ and Cu $2p_{1/2}$, arising from spin–orbit coupling. Both the 3 and 10 wt% films exhibit these main peaks; however, the Cu 2p spectra of the 3 wt% sample are relatively noisy and do not clearly display satellite features. This can be attributed to the lower Cu content compared to Ni and O, as well as the higher Cu concentration in the 10 wt% sample, which enhances the visibility of the satellite peaks.

The Cu $2p_{3/2}$ peak is observed at 932.56 eV (3 wt%) and 932.60 eV (10 wt%), while the Cu $2p_{1/2}$ peak appears at 952.23 eV (3 wt%) and 952.32 eV (10 wt%).[31,32] The two peaks are separated by 19.67 eV (3 wt%) and 19.76 eV (10 wt%), consistent with the expected spin–orbit splitting values. In the 10 wt% Cu–NiO film, characteristic Cu $2p_{3/2}$ satellite features are identified at ~940.80 eV and ~943.35 eV, along with a shoulder near 953.73 eV in the Cu $2p_{1/2}$ region[27] and a Cu $2p_{1/2}$ satellite peak at ~961.56 eV.[27] These satellite features confirm the presence of Cu^{2+} in its ground state with a d^9 electronic configuration, consistent with the main Cu $2p_{3/2}$ peak typically observed around 932.4 eV.[33]

3.6. AFM analysis

Fig. 10 presents 3D surface images obtained using NanoScope Analysis software to evaluate the surface morphology and roughness of Cu-doped NiO thin films. The undoped sample exhibits a well-defined grain structure with particles appearing

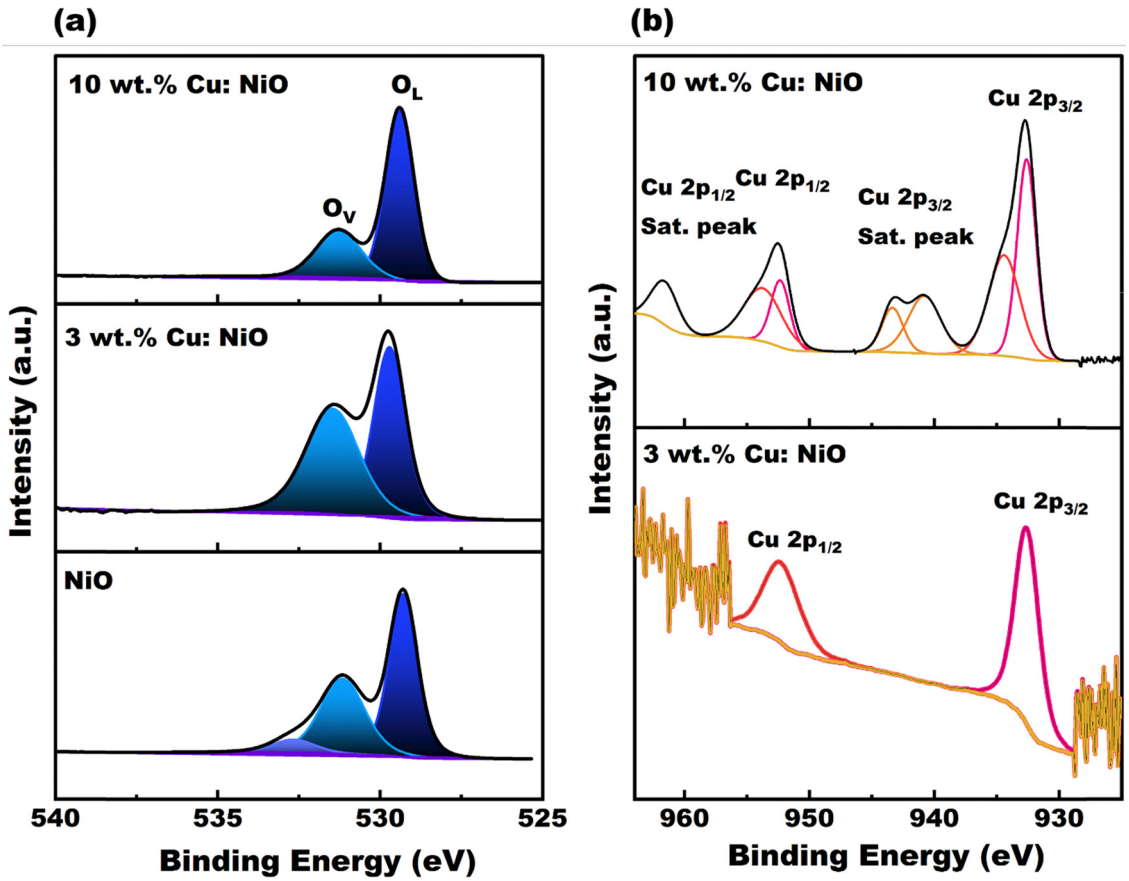

Fig. 9 (a) O 1s core-level spectra of pristine NiO, 3 wt%, and 10 wt% Cu–NiO thin films; (b) Cu 2p spectra of 3 wt% and 10 wt% Cu–NiO thin films.

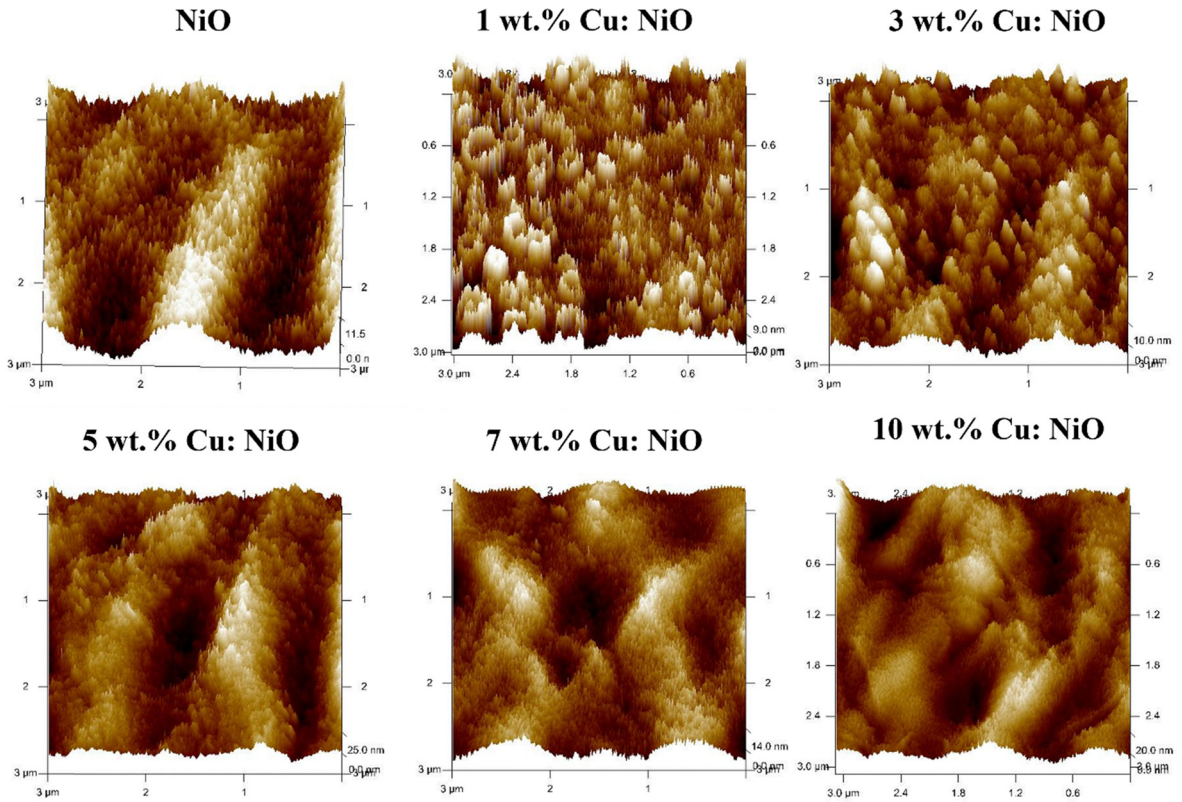

Fig. 10 The topographical images of Cu–NiO thin films.

in a strip-like form, indicative of orderly grain growth. Upon Cu doping, notable morphological changes are observed. The 1 wt% and 3 wt% doped samples show visible agglomeration, while higher doping levels (5–10 wt%) exhibit finer granular grains with greater surface height variations.

A gradual variation in surface roughness was observed in Cu–NiO films. The roughness values were 3.81, 2.34, 2.44, 5.96, 3.46, and 4.79 nm corresponding to pristine, 1%, 3%, 5%, 7%, and 10% Cu concentrations, respectively, values that remain within the acceptable range for NLO measurements. An overall increase in surface roughness is observed with doping, though a non-linear trend is evident. The roughness increases up to 5 wt% Cu, then slightly decreases at 7 wt%, before rising again at 10 wt% similar behavior was observed in Cu-doped NiO films, as previously reported in the literature.[20,34]

This variation in surface roughness can be attributed to several factors. Cu doping tends to reduce crystallite size, leading to an increased number of grain boundaries. These boundaries introduce surface irregularities, contributing to roughness enhancement. Additionally, doping induces structural defects such as dislocations and vacancies, which further disrupt surface uniformity.[21] Collectively, these factors account for the observed fluctuations in surface roughness.

While increased surface roughness enhances the effective surface area, potentially improving light absorption, excessive roughness can scatter the incident beam and reduce the efficiency of the NLO response. Therefore, an optimal balance between surface morphology and doping concentration is essential for achieving desirable optical performance.

3.7. THG by varying the fluence

The third harmonic generation measurement was executed to accurately quantify the third-order nonlinearity that develops purely from the electronic contributions of the material. This technique eliminates nonlinearity from thermal, mechanical, and orientational effects, thus providing a measurement that reflects only the electronic nonlinearity of the medium.

Fig. 11 illustrates the variation of the THG signal with fluence for Cu–NiO thin films at different Cu doping concentrations. A non-monotonous behavior in the THG signal is observed with changes in Cu content. For lower Cu doping levels, such as 1 wt%, the THG signal appears even at low fluence values (*e.g.*, 61.2 J m^{-2}). However, as the Cu concentration increases, the THG signal is not detected at these lower fluences. Nevertheless, when the fluence increases from 61.2 J m^{-2} to 149.2 J m^{-2}, a clear increase in the THG signal is observed across all samples, regardless of Cu concentration.

In this study, the THG signal shows a distinct dependence on the dopant concentration. Among the doped samples, the 1 wt% sample exhibits the highest THG signal, even surpassing that of the pristine sample. The sample with 3 wt% doping also shows enhanced THG response compared to pristine, although slightly lower than the 1 wt% sample. Interestingly, the sample with 5 wt% doping exhibits a THG intensity nearly identical to that of the pristine sample. However, with further increase in

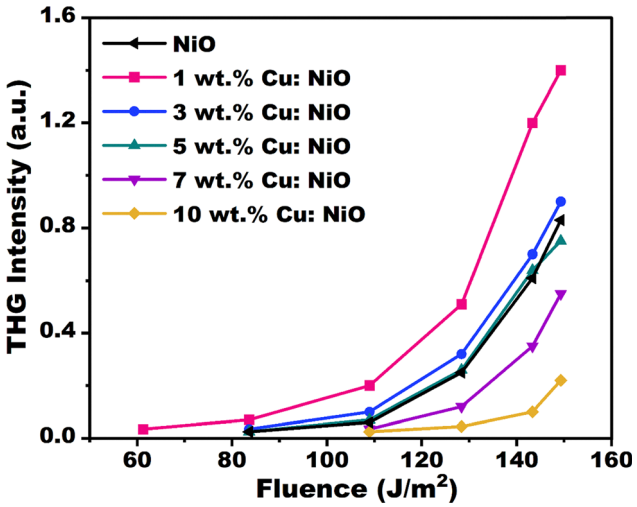

Fig. 11 Fluence-dependent THG response of Cu–NiO thin films.

dopant concentration to 7 wt% and 10 wt%, a noticeable reduction in THG signal is observed, falling below that of the pristine sample. This behavior suggests that low doping levels induce beneficial structural modifications, which, upon interaction with the nanosecond excitation laser, enhance the THG response. In contrast, higher doping concentrations introduce excessive defect formation and structural disorder, which deteriorate the nonlinear optical performance.

The presented results show that the 1 wt% Cu-doped NiO samples exhibit the highest NLO responses. This enhanced THG efficiency can be attributed to the optimal structural modifications induced at this doping level, where the dipole moments in both ground and excited states attain favorable values due to the specific arrangement and spacing of nanostructures dictated by Cu concentration.[35] Additionally, the orientation of crystalline growth, nano-grain morphology, and their spatial distribution significantly influence the optical response. The increased THG efficiency could be attributed to the defect states introduced by Cu doping, which enhances photoexcitation and relaxation processes in the material, contributing to the overall THG performance. Furthermore, in the nanosecond regime, resonance effects, particularly two-photon resonances, can significantly boost efficiency when the laser frequency aligns with specific energy level transitions in the material. These linear and nonlinear interactions are more effectively facilitated by longer pulse durations, resulting in the highest THG efficiency observed under nanosecond excitation. The increased THG efficiency likely results from a combination of defect-induced localized states, enhanced multiphoton absorption,[36] and photo-polarization effects induced by the nanosecond pulsed laser, all of which contribute synergistically to the observed nonlinear optical performance.

3.8. THG by Makers fringe technique

To measure the third-order nonlinear susceptibility of materials, the THG experiment was performed using the Maker fringes method through a comparative model.[37] This model relies on comparing the maximum intensity of the generated third-harmonic signal from the studied material to that of a reference. In this study, fused silica was used as the reference material for the THG experiment. Since linear absorption at the third-harmonic wavelength is significant, the calculation of third-order susceptibility includes the linear absorption coefficient. The experimental results were evaluated using the Kubodera and Kobayashi model,[37–39] which defines the third-order nonlinear susceptibility, $\chi^{(3)}$, through the following equation:

$$\chi^{(3)} = \chi_s^{(3)} \left(\frac{2}{\pi}\right) l_{C,S} \left(\frac{\frac{\alpha}{2}}{1 - e^{-\frac{\alpha l}{2}}}\right) \left(\frac{I^{3w}}{I_S^{3w}}\right)^{\frac{1}{2}} \quad (8)$$

The reference material's third-order nonlinear susceptibility, denoted as $\chi_s^{(3)}$, has a known value of 2.0×10^{-22} m^2 V^{-2}.[40] In cases where the sample's thickness l is significantly smaller than the coherence length $l_{C,S}$ (6.7 μm for the fused silica reference), phase-matching conditions are effectively satisfied. The peak intensities of the third-harmonic signals generated by the sample and the reference are represented by I^{3w} and I_S^{3w}, respectively. Additionally, the linear absorption coefficient at the wavelength of 355 nm is represented by α. The measured values of $\chi^{(3)}$ for the Cu-doped NiO thin films are summarized in Table 2.

Fig. 12 presents the THG signal as a function of the incident angle for the Cu–NiO thin films under the fundamental laser beam. The experimental results showed that the THG intensity exhibited oscillations with changes in the laser beam's incidence angle. The signal intensity was influenced by the Cu doping concentration. The THG signals were symmetrical for both samples, indicating smooth surfaces and good film quality.[41] Strong interference fringes are absent, mainly because the film thickness is smaller than the coherence length. However, THG still occurs, though the signal is generally weaker due to the thin film. The intensity varies smoothly with angle, showing slight oscillations and angular dependence without prominent fringes.

The THG response increases from pristine to 3 wt% Cu–NiO, with the 3 wt% sample showing the highest intensity. This sample exhibits noticeable increases in THG intensity with higher incident angles. However, further increasing the doping concentration to 5 and 10 wt% leads to a reduction in the THG signal. The Cu-doped sample with 3 wt% NiO exhibited the highest THG response. This enhancement is attributed to the interaction of the picosecond laser with the materials at its optimized doping level, which effectively increases free carrier concentration and promotes efficient charge transfer within

Table 2 Third-order NLO susceptibilities obtained from experimental studies using the Maker fringe technique

Cu dopant concentration (wt%)	$\alpha \times 10^6$ (m^{-1})	$\chi^3 \times 10^{-21}$ (m^2 V^{-2})
NiO	6.28	7.00
1 wt% Cu:NiO	6.67	7.54
3 wt% Cu:NiO	7.10	7.61
5 wt% Cu:NiO	9.32	6.98
7 wt% Cu:NiO	10.2	5.68
10 wt% Cu:NiO	11.8	4.55

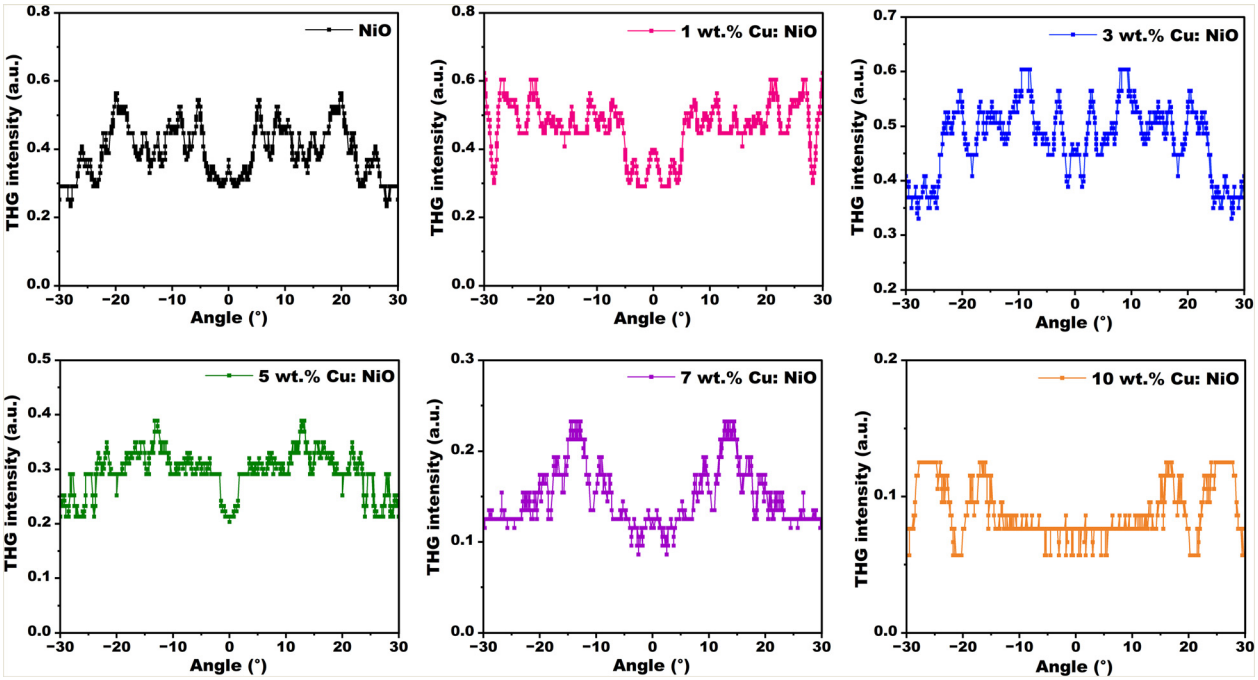

Fig. 12 Variation of THG intensity with incident angle for Cu–NiO thin films.

the thin film. Additionally, doping at this concentration can introduce favorable defect states that further improve nonlinear optical properties by enhancing carrier mobility and polarization response. Moreover, the interaction of the material with short-pulse laser excitation highlights the influence of electronic structure and ultrafast carrier dynamics, where rapid excitation and relaxation processes contribute significantly to the observed nonlinear response. The combination of these factors, optimized charge transport, increased free carriers, controlled defect density, and dynamic carrier behavior under ultrafast excitation, leads to a markedly stronger THG signal.

However, beyond this optimal doping level (above 3 wt%), excessive Cu incorporation can introduce significant lattice strain and structural distortion, leading to degraded crystallinity and a reduction in the crystallite size.[42] This results in a decrease in THG efficiency at higher doping levels. These findings suggest that careful control of doping concentration, especially in thin films, is crucial for maximizing nonlinear optical performance, making such materials promising for advanced optical and photonic technologies.

A comparative analysis of χ^3 values for thin films prepared by different chemical deposition methods is presented in Table 3. All the χ^3 values listed were determined using the Maker fringes technique, ensuring consistency in measurement. This comparison emphasizes the key contribution of the synthesis route in influencing the nonlinear optical response of thin films, likely due to variations in structural, morphological, and optical properties induced by the respective deposition techniques.

Table 3 Comparison of third-order nonlinear susceptibility values of thin films synthesized by various chemical deposition techniques, measured using the Maker fringes technique

Materials (thin film)	Method	$\chi^3 \times 10^{-21}$ ($m^2 V^{-2}$)	Ref.
NiO	Spray pyrolysis	1.94	43
NiO:Sn (1%)	Spin coating	3.13	42
7% Zn-doped MgO	Dip coating	4.028	44
Fe-doped CuO	Spin coating	2.90	45

3.9. Z-scan technique

The third-order nonlinear optical parameters, such as nonlinear absorption, nonlinear refraction, and third-order susceptibility, were determined using the simple single-beam Z-scan technique proposed by Sheik Bahe.[46] Both open-aperture and closed-aperture Z-scan measurements were performed to determine the sign and magnitude of the sample's nonlinear absorption and nonlinear refractive index. From these results, the real and imaginary parts of the third-order susceptibility were calculated. In the experiment, a continuous-wave He–Ne laser was used as the excitation source. The laser beam was focused onto the sample using a convex lens, and the transmitted intensity was recorded as a function of sample position. Open-aperture measurements were performed without an aperture in front of the detector, while closed-aperture measurements involved placing an aperture to analyze the nonlinear refraction.

The normalized transmittance, T,[46] obtained from the open-aperture Z-scan measurements, was fitted using eqn (9), where z represents the sample position relative to the focal plane, z_R is the Rayleigh length of the focused beam (calculated as 6.11 mm), L_{eff} is the effective thickness of the sample $\left(L_{eff} = \frac{1 - e^{-\alpha L}}{\alpha}\right)$, L is the thickness of the prepared sample ($\sim$300 nm), I_0 denotes the intensity at the focal point

(calculated as 1.03×10^7 W m^{-2}), and λ is the wavelength of the incident beam, which was 633 nm in this experiment.

$$T(z) = 1 - \frac{\beta_{\text{eff}} I_0 L_{\text{eff}}}{(2)^{\frac{3}{2}}\left(1 + \frac{z^2}{z_R{}^2}\right)} \quad (9)$$

The OA curves of the Cu-doped NiO thin films are represented in Fig. 13. All films exhibit reverse saturable absorption (RSA), where transmittance decreases with increasing laser intensity, indicating positive nonlinear absorption behavior. RSA typically occurs when the absorption cross-section of the excited state exceeds that of the ground state, leading to stronger absorption at higher intensities. The varying depths of the transmittance dips among the samples clearly reflect differences in their intensity-dependent optical absorption capabilities.

The observed nonlinear absorption arises from the interplay of multiple mechanisms, including resonant and non-resonant processes. Resonant nonlinearities involve real electronic transitions near the laser excitation energy, as evident from the absorbance spectra of the films, and are associated with relatively slower dynamics. Non-resonant mechanisms, on the other hand, involve defect states or virtual energy levels and contribute through multiphoton absorption processes, which are generally faster.[41]

In these Cu-doped NiO thin films, two-photon absorption (TPA) is a key contributor to the nonlinear response. Both genuine (simultaneous) and sequential TPA processes are possible under the 633 nm laser excitation (1.96 eV), given that the photon energy exceeds half of the material's bandgap. In sequential TPA, one-photon absorption excites electrons to an intermediate state, followed by further absorption to reach higher energy states. This process, along with thermally induced excited-state absorption (ESA), plays a significant role in the RSA behavior observed.

Additionally, the role of free carriers is particularly significant in these semiconductor thin films. Cu doping increases the free carrier concentration, enhancing the material's capacity to absorb photons through free-carrier absorption (FCA), which in turn contributes to additional absorption pathways. Notably, the nonlinear optical response is not solely due to free carriers; rather, FCA-assisted TPA processes play a crucial role in driving the observed nonlinear absorption behavior.

The energy-level diagram of Cu-doped NiO thin films (Fig. 14) highlights several defect states within the bandgap, such as near band edge states (3.1 eV), Ni interstitials (2.92 eV), nickel vacancies (2.79 eV and 2.64 eV), oxygen vacancies (2.17 eV), and oxygen interstitials (2.03 eV). The laser photon energy (1.96 eV) closely matches oxygen-related defect levels, facilitating resonant absorption through these shallow states. Simultaneously, under high-intensity excitation, TPA processes (1.96 eV + 1.96 eV = 3.92 eV) promote electron transitions to the conduction band or higher energy levels. Therefore, the enhanced nonlinear optical absorption in these films results from a combined effect of resonant defect-assisted absorption, TPA, thermally induced ESA, and FCA mechanisms.

The incorporation of transition metal dopants, such as Cu, into NiO thin films significantly enhances their NLO properties. The pristine NiO sample displays a moderate transmittance dip under high-intensity illumination, while the 1 wt% Cu-doped NiO film exhibits the deepest dip, indicating the strongest RSA effect. This pronounced RSA response

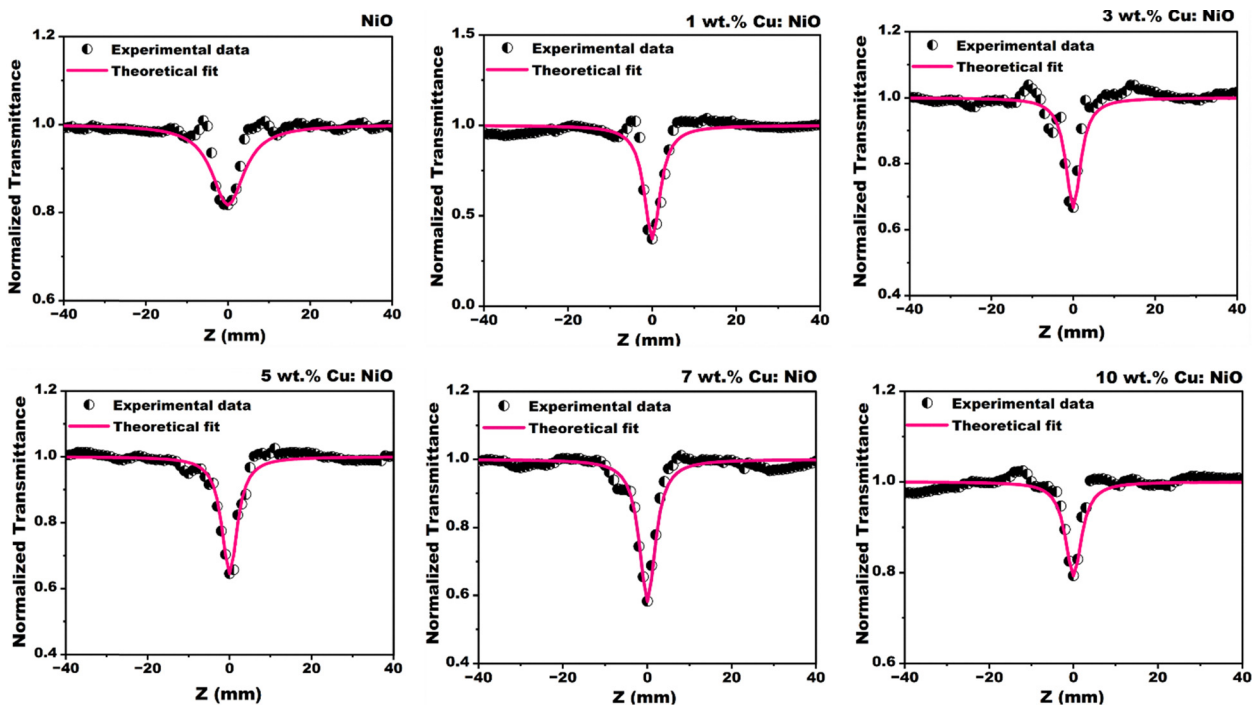

Fig. 13 OA Z scan traces of Cu–NiO thin films.

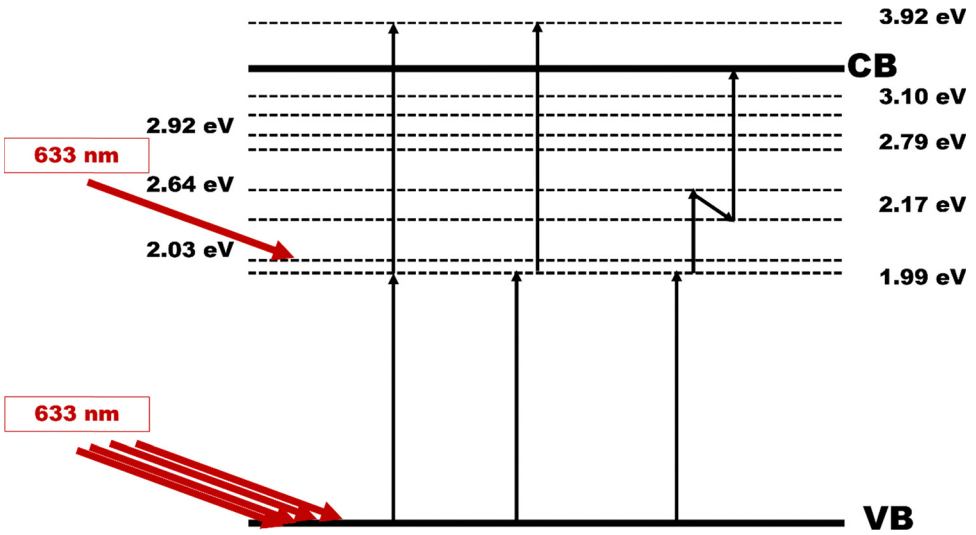

Fig. 14 Energy level diagram illustrating the genuine and sequential two-photon absorption mechanism in Cu-doped NiO thin films.

underscores the suitability of Cu–NiO films in optical limiting applications, especially in protecting sensitive optical components from high-intensity laser radiation.

The enhancement in RSA can be linked to the introduction of new intermediate energy levels within the bandgap due to Cu doping. These defect states promote nonlinear absorption mechanisms such as multi-photon absorption and excited-state transitions. Among the doped films, the 1 wt% Cu-doped sample demonstrates the highest β, suggesting that this doping level provides an optimal balance of structural and electronic modifications.

As shown in Fig. S7, the maximum possible error associated with the OA Z-scan curve measurements is presented, indicating that the observed variations are within an acceptable range and support the reliability of this observation. The superior crystallinity, smoother surface morphology, and nanometer-scale crystallite size in the 1 wt% Cu-doped film likely contribute to its enhanced NLO response.

However, increasing the Cu content beyond 1 wt% leads to increased lattice distortions and structural imperfections, introducing strain within the film. These defects may disrupt the electronic structure and negatively impact on the RSA process, resulting in a reduced β value. Despite this, all Cu-doped samples still exhibit higher β values than the pristine NiO film, affirming that Cu incorporation is beneficial for improving NLO behavior.

In summary, classical Cu doping in NiO thin films emerges as an effective strategy to enhance nonlinear optical absorption. The observed improvement is primarily due to dopant-induced defect states, new electronic levels within the bandgap, and enhanced free carrier absorption. These results highlight the critical role of optimized doping concentration in tailoring materials for advanced nonlinear optical applications.

In the closed-aperture (CA) Z-scan configuration, it is used to determine the sign and magnitude values of the nonlinear refractive index and real third-order susceptibility of the material. In a typical closed-aperture Z-scan measurement, the recorded signal comprises contributions from both nonlinear absorption and nonlinear refraction. To extract the pure nonlinear refractive component, the influence of nonlinear absorption must be eliminated. This is commonly achieved by normalizing the closed-aperture data with the corresponding open-aperture data.

The normalized transmittance T is theoretically evaluated based on the sample displacement and the nonlinear refractive index, based on the analytical expressions provided in ref. 46. The transmittance is given by:

$$T = 1 - \frac{4 \times x \times \Delta\phi_0}{\left(\frac{z^2}{z_R{}^2} + 1\right)\left(\frac{z^2}{z_R{}^2} + 9\right)} \quad (10)$$

In this expression, $\Delta\phi_0$ represents the on-axis nonlinear phase shift, which is calculated using:

$$\Delta\phi_0 = \frac{\Delta T_{p-v}}{0.406(1-s)^{0.25}} \quad (11)$$

Here, ΔT_{p-v} denotes the difference between the peak and valley transmittance values in the CA Z-scan trace, and s refers to the linear transmittance of the aperture, which is set at 0.7 for the present case. The nonlinear refractive index n_2 (in SI units of $m^2\ W^{-1}$) is then computed from the phase shift using the relation:[47]

$$n_2\ (m^2\ W^{-1}) = \frac{\Delta\phi_0 \lambda}{2\pi L_{eff} I_0} \quad (12)$$

The CA Z-scan traces of Cu–NiO thin films are given in Fig. 15. All samples display a peak-to-valley profile, indicating self-defocusing behavior and a negative nonlinear refractive index (n_2).

The value of n_2 depends on the various factors, such as electronic polarization, free carrier absorption, nonlinear scattering, and thermal effect.[47] In this case, thermal effects

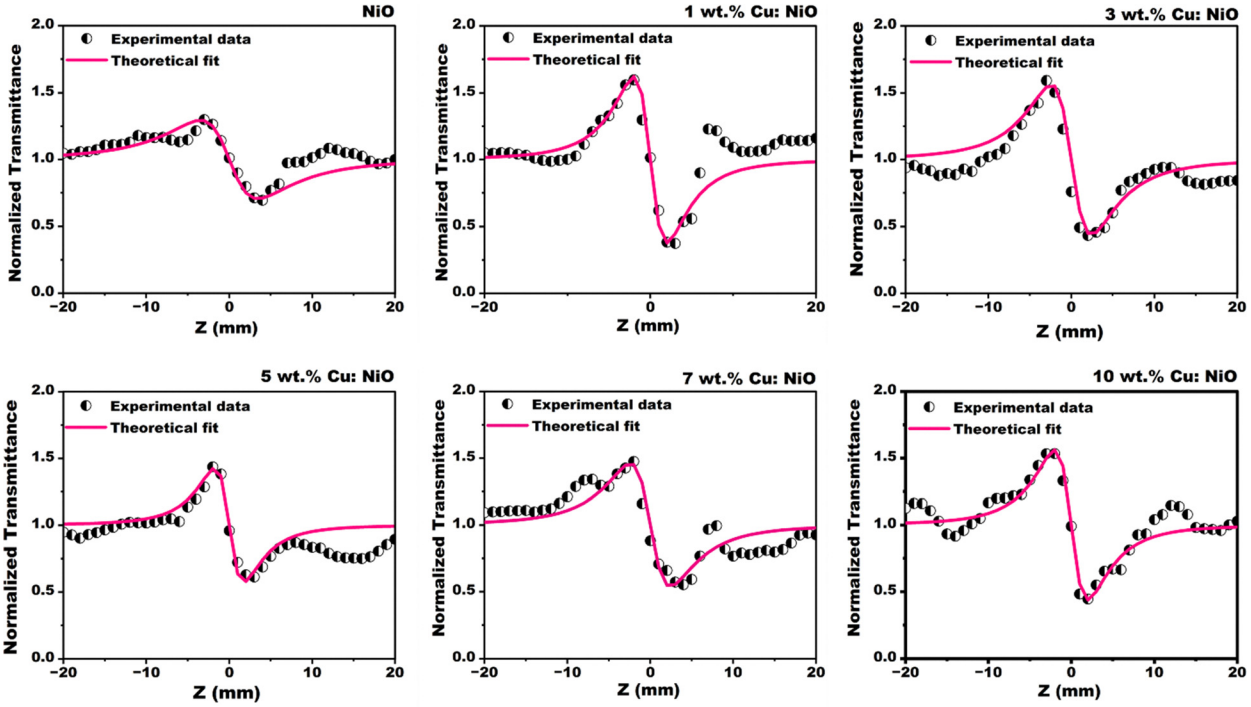

Fig. 15 CA Z-scan traces of Cu–NiO thin films.

dominate due to energy absorption from 633 nm CW laser exposure. Continuous illumination leads to localized heating in the dispersed system, causing density changes and spatial variation in the refractive index. This thermally induced modulation gives rise to a lens-like optical behavior. Thus, the thermal contribution is considered the primary driver of the nonlinearity observed. The trend indicates a negative nonlinear refractive index, suggesting a self-defocusing response in the material.

Furthermore, over 1.7 times the Rayleigh length is exceeded by the graph's peak–valley separation, which implies that the thermal nonlinear mechanism is responsible for the observed nonlinearity. This behavior confirms that thermal effects play a significant role in the self-defocusing characteristics of the CuNiO nanostructure films.

The enhancement in the nonlinear parameters upon Cu doping is due to the increased defect centers in the lattice and the increased nonlinear refractive coefficient due to the thermal local heating. The morphological alteration caused by densification and coalescence leads to better particle connectivity, which facilitates more efficient heat dissipation, thereby contributing to a stronger thermal lensing effect.[48]

The increase in Cu doping enhances the number of optically active centers involved in the NLO processes, thereby contributing to an increase in the n_2. PL spectra show a rise in intensity at 1 wt% doping, which indicates an increase in defect states. These defects promote localized heating due to thermal agitation, leading to a thermally induced enhancement in the nonlinear refraction. At doping levels beyond 1 wt%, a reduction in the n_2 is initially observed, possibly due to a decrease in defect centers or quenching effects, as suggested by the drop in PL intensity. However, with further increase in doping, n_2 shows a gradual rise. This enhancement is likely driven by the formation of non-radiative defect states, which contribute to NLO effects through mechanisms such as excited-state absorption and thermal lensing, ultimately leading to variations in the n_2.

Following this, the third-order nonlinear optical susceptibility χ^3 is determined by evaluating both its real and imaginary components. These are derived from the nonlinear refractive index n_2 and the effective nonlinear absorption coefficient β, respectively, as described in ref. 49:

$$\mathrm{Re}\ \chi^3\ (\mathrm{m}^2\ \mathrm{V}^{-2}) = 2{n_0}^2\varepsilon_0 c n_2 \quad (13)$$

$$\mathrm{Im}\chi^3\ (\mathrm{m}^2\ \mathrm{V}^{-2}) = \frac{{n_0}^2\varepsilon_0 c\lambda}{2\pi}\beta \quad (14)$$

In these equations, ε_0 represents the vacuum permittivity, n_0 refers to the material's linear refractive index, and c indicates the velocity of light in free space. The calculated values of the nonlinear refractive index (n_2), nonlinear absorption coefficient (β), and third-order susceptibility components are listed in Table 4. The nonlinear optical parameters exhibit higher values in Cu–NiO thin films compared to the pristine NiO sample, indicating enhanced involvement of dopant ions in the NLO processes. Among all samples, the 1 wt% Cu-doped NiO film exhibits the highest values.

Several research groups have reported diverse nonlinear optical responses in doped NiO systems under different excitation conditions. For example, N-doped NiO and Cu-doped NiO investigated with a He–Ne laser (632.8 nm, CW) exhibited β

Table 4 NLO parameters values of Cu–NiO thin films

Cu dopant concentration (wt%)	$\beta_{eff} \times 10^{-1}$ (m W^{-1})	$n_2 \times 10^{-7}$ (m^2 W^{-1})	Re $\chi^3 \times 10^{-9}$ (m^2 V^{-2})	Im $\chi^3 \times 10^{-10}$ (m^2 V^{-2})	$\chi^3 \times 10^{-9}$ (m^2 V^{-2})
NiO	2.35	−0.66	−1.69	3.01	1.72
1 wt% Cu:NiO	8.30	−1.45	−3.70	10.7	3.86
3 wt% Cu:NiO	4.07	−1.20	−3.09	5.26	3.13
5 wt% Cu:NiO	4.59	−0.97	−2.53	6.01	2.60
7 wt% Cu:NiO	5.23	−1.01	−2.67	6.93	2.76
10 wt% Cu:NiO	2.71	−1.29	−3.54	3.74	3.56

values in the 10^{-4} m W^{-1} range[49,50] while Cu–NiO studied under Nd:YAG laser excitation (532 nm, CW) showed much higher β on the order of 10^{-3} m W^{-1}.[51] In contrast, Cr-doped NiO displayed significantly lower nonlinear coefficients, with β values around 10^{-6} m W^{-1}.[52] These reports indicate that both the dopant type, concentration, and laser source strongly influence the magnitude of β and n_2. Compared with these earlier findings, the present study demonstrates remarkably enhanced nonlinear absorption, confirming the superior NLO performance of the prepared Cu–NiO thin films.

The comparative analysis of recently reported results of third-order nonlinear optical coefficients (β and n_2) presented in Table 5 demonstrates that the Cu-doped NiO thin films synthesized in this study exhibit superior nonlinear absorption and refraction compared with several reported metal-oxide nanostructures under continuous-wave excitation. The observed β value (8.30×10^{-1} m W^{-1}) is significantly higher than those of Cr_2O_3, MgO, and Bi^{3+}-doped $MnWO_4$ systems, indicating strong nonlinear absorption arising from Cu-induced defect states enhanced charge-transfer interactions within the NiO lattice. These results confirm the enhanced nonlinear optical response of Cu–NiO relative to other oxide-based nanomaterials, highlighting its potential for optical limiting and photonic device applications.

The enhanced third-order nonlinear optical performance of Cu-doped NiO thin films arises from the combined effects of Cu substitution, defect modulation, and localized electronic states. The incorporation of Cu^{2+} ions (ionic radius 0.72 Å) in place of Ni^{2+} (0.69 Å) induces a slight lattice distortion, which facilitates the formation of oxygen vacancies (O_V) and Ni^{3+} ions to maintain charge neutrality. These O_V defects introduce additional localized states within the bandgap, resulting in bandgap narrowing, as observed from Tauc's analysis. The impurity states further modify the electronic structure through sp–d exchange interactions between Cu 3d electrons and conduction-band electrons, as well as d–d exchange interactions between the localized 3d electrons of Cu^{2+} and Ni^{2+} ions, promoting intraband and defect-level transitions under laser excitation. Furthermore, Cu doping reduces the optical bandgap and enhances the carrier density, thereby increasing polarizability and charge-transfer interactions between Ni^{2+}/Cu^{2+} and O^{2-} ions. This leads to stronger nonlinear polarization and enhanced nonlinear refractive index (n_2) and nonlinear absorption coefficient (β) values, resulting in an enhanced third-order nonlinear susceptibility (χ^3). Therefore, the synergistic influence of Cu-induced defect states, enhanced charge transfer, and lattice distortion contributes to the observed improvement in third-order nonlinear optical performance.

3.10. Summary of nonlinear optical studies

This research explores the multifunctional behavior of Cu–NiO films aimed at advanced nonlinear optics-based applications. Third-harmonic generation efficiency of the films was investigated under two excitation conditions:

(1) Nanosecond laser excitation at varying fluence levels.

(2) Picosecond laser excitation by varying the rotational angle of incidence.

The results indicate that:

• Under nanosecond excitation, the 1 wt% Cu-doped film exhibited the highest THG, attributed to combined linear and nonlinear mechanisms due to the longer pulse interaction.

• Under picosecond excitation, the 3 wt% Cu-doped film showed the strongest THG, highlighting the influence of electronic properties and ultrafast dynamics in short-pulse regimes.

The variation in THG efficiency across different doping levels and excitation conditions is primarily governed by the

Table 5 Reported β and n_2 values for metal oxide nanomaterials under CW laser excitation

Material	Laser parameter	β (m W^{-1})	n_2 (m^2 W^{-1})	Ref.
$Zn_{0.96}Cr_{0.04}O$	Diode laser (532 nm)	3.00×10^{-6}	3.23×10^{-13}	53
5 wt% Cd-doped CuO–PVA	He–Ne laser (632.8 nm)	1.10×10^{-7}	38.9×10^{-9}	54
6% Ni-doped CuO	CW DPSS laser (532 nm)	1.92×10^{-7}	3.446×10^{-4}	55
CuO	Diode laser (532 nm)	1.38×10^{-4}	-2.01×10^{-9}	56
Bi^{3+} (0.7%) doped $MnWO_4$	Nd:YAG laser (532 nm)	1.18×10^{-6}	4.95×10^{-13}	57
Cr_2O_3	Nd:YAG laser (532 nm)	3.75×10^{-3}	3.24×10^{-9}	58
Co (0.05) doped MgO	Nd:YAG laser (532 nm)	3.06×10^{-6}	5.75×10^{-13}	59
1 wt% Cu:NiO	He–Ne laser (632.8 nm)	8.30×10^{-1}	-1.45×10^{-7}	Present work

interaction time of the laser with the material, affecting excitation and relaxation dynamics.

In addition, Z-scan measurements were performed to analyze third-order nonlinearity through nonlinear absorption and nonlinear refraction.

The maximum value of third-order susceptibility (χ^3) was observed for the 1 wt% Cu-doped sample under continuous-wave excitation, consistent with THG results under nanosecond excitation. This enhanced response is primarily due to thermally induced excited-state absorption and nonlinear refraction, associated with thermal lensing effects.

The discrepancy between the χ^3 values obtained from the Maker fringe technique and the Z-scan measurements primarily arises from the different nature of their laser–material interactions. In the Maker fringe technique, the interaction involves picosecond laser pulses, emphasizing electronic nonlinearities and ultrafast carrier dynamics. Additionally, this technique is comparative in nature, relying on reference materials for χ^3 estimation. In contrast, the Z-scan technique, particularly under continuous-wave laser excitation, is more sensitive to thermally induced nonlinear effects, which can significantly contribute to the higher χ^3 values observed.

Overall, these results confirm the strong third-order nonlinear behavior of Cu-doped NiO films and demonstrate their potential for applications in photonic devices operating under various pulsed and CW regimes.

4. Conclusion

Cu-doped NiO thin films were successfully fabricated *via* spray pyrolysis and systematically investigated for their structural, linear, and nonlinear optical properties. Structural and linear optical analysis confirmed that Cu incorporation influenced crystallinity and introduced defect states, which in turn played a pivotal role in enhancing the optical response. Photoluminescence and XPS analyses further verified the presence of nickel- and oxygen-related defects, establishing a clear link between defect engineering and the observed nonlinear behavior.

The nonlinear optical characterization revealed that Cu doping significantly strengthened the third-order nonlinear response. Under nanosecond excitation, pronounced THG was observed, with intensity scaling consistently with fluence, primarily due to defect-assisted localized states, enhanced multiphoton absorption, and photo-polarization effects. In contrast, under picosecond excitation, THG performance depended strongly on both angle and Cu concentration, emphasizing the role of ultrafast carrier dynamics and optimized charge transport. Together, these effects led to a measurable increase in χ^3 values from 7.00×10^{-21} to 7.61×10^{-21} $m^2 V^{-2}$ with Cu incorporation. Complementary Z-scan analysis confirmed reverse saturable absorption and thermally induced self-defocusing, further demonstrating the negative nonlinear refractive index and strong third-order susceptibility enhancement.

Overall, the findings establish a direct correlation between Cu-induced structural/electronic modifications and the improved nonlinear optical response. These results position Cu–NiO thin films as promising candidates for advanced photonic applications such as optical limiting, laser protection, and nonlinear optical devices. Future studies should focus on optimizing excitation regimes (particularly femtosecond lasers) and integrating these films into device architectures to fully exploit their multifunctional potential.

Conflicts of interest

There are no conflicts to declare.

Data availability

The data cannot be made publicly available upon publication as they are not available in a standard format that is sufficiently accessible by other researchers. The data that support the outcomes of this study will be shared upon reasonable request from the authors.

Acknowledgements

The authors would like to acknowledge the Sophisticated Analytical Instrument Facility (SAIF), Manipal University, Jaipur, for XRD and Raman Measurements. The presented results are part of the TeraHertz project that has received funding from the HORIZON-MSCA-2021-SE-01 Program, agreement number 101086493. Katarzyna Ożga (K. O.) and Jarosław Jędryka (J. J.) acknowledged the project cofinanced by the Polish Ministry of Education and Science under the program ''Co-financed international projects'', project no. W26/HE/2023 (Dec. MEiN 5451/HE/2023/2).

References

1 P. Chaiworn, W. Teerananattapong, P. Reunchan, A. Tubtimtae and E. Wongrat, Effect of tungsten oxide concentration on structural, morphological, compositional, dispersion energy, and linear/nonlinear optical properties of niobium pentoxide thin films, *Opt. Mater.*, 2025, **161**, 116807, DOI: 10.1016/j.optmat.2025.116807.

2 N. Suwannakham, A. Tubtimtae and E. Wongrat, Structural, linear/non-linear optical, optoelectrical, and electrical properties of novel crystalline antimony-doped tin oxide thin films synthesized by the chemical deposition method, *Phys. B*, 2023, **649**, 414440, DOI: 10.1016/j.physb.2022.414440.

3 Y. Pepe, B. A. Unlu, S. Akkoyun, N. Asci, A. Karatay and A. Ates, *et al.*, Optical Limiting Performance of Titanium Dioxide-Filled Polyvinylpyrrolidone Composite Nanofibers, *ACS Omega*, 2025, **10**, 23049–23057.

4 A. L. Jadhav, S. L. Jadhav, S. Mali, C. K. Hong and A. V. Kadam, 3D marigold flowers of copper-nickel oxide composite materials as a positive electrode for high-performance hybrid supercapacitors, *New J. Chem.*, 2024, **48**, 12275–12287.

5 S. K. Sinha, B. Kumar, R. Kumar, S. Ganguly and A. Hazra, Synthesis and characterization of hybrid NiO/CeO2 p-n heterojunction nanofibers for room temperature ammonia sensing application, *Surf. Interfaces*, 2024, **51**, 104568, DOI: 10.1016/j.surfin.2024.104568.
6 H. Yang, Y. Hu, X. Yin, J. Huang, C. Qiao and Z. Hu, *et al.*, A disposable and sensitive non-enzymatic glucose sensor based on a 3D-Mn-doped NiO nanoflower-modified flexible electrode, *Analyst*, 2022, **148**, 153–162.
7 S. Liu, J. Jia, J. Wang, S. Liu, X. Wang and H. Song, *et al.*, Journal of Magnetism and Magnetic Materials Synthesis of Fe-doped NiO nanofibers using electrospinning method and their ferromagnetic properties, *J. Magn. Magn. Mater.*, 2012, **324**, 2070–2074, DOI: 10.1016/j.jmmm.2012.02.017.
8 T. Jia, Y. Hao, X. Qi, Y. Rao, L. Wang and J. Ding, *et al.*, Interface engineering and impedance matching strategy to develop core@shell urchin-like NiO/Ni@carbon nanotubes nanocomposites for microwave absorption, *J. Mater. Sci. Technol.*, 2024, **176**, 1–12.
9 M. Kumar, Effect of substrate temperature on surface morphology and optical properties of sputter deposited nanocrystalline nickel oxide films, *Mater. Res. Express*, 2019, **6**(9), 096404, DOI: 10.1088/2053-1591/ab2af2.
10 A. Laib, A. Benhaoua, M. L. Ayachi, S. E. Laouini and M. L. Tedjani, Effect of Li doping on the structural, linear and nonlinear optical properties of NiO thin films, *Ferroelectrics*, 2022, **599**, 186–200, DOI: 10.1080/00150193.2022.2113651.
11 M. S. Bannur, A. Antony, K. I. Maddani, P. Poornesh, A. Rao and K. S. Choudhari, Tailoring the nonlinear optical susceptibility $\chi(3)$, photoluminescence and optical band gap of nanostructured SnO2 thin films by Zn doping for photonic device applications, *Phys. E*, 2018, **103**, 348–353.
12 C. Rajashree, A. R. Balu, K. Arunkumar, Z. Delci, C. Kayathiri and M. Karthika, *et al.*, Continuous wave laser induced nonlinear optical, optoelectronic and magnetic properties of Co2+ ions substituted (Mg + Ag) doped CdO thin films, *J. Alloys Compd.*, 2025, **1035**, 181481, DOI: 10.1016/j.jallcom.2025.181481.
13 A. Javadian and M. R. Fadavieslam, Impact of copper doping in NiO thin films deposited by spray pyrolysis on their physical properties, *J. Mater. Sci.: Mater. Electron.*, 2022, **33**, 23362–23374, DOI: 10.1007/s10854-022-09098-5.
14 R. Thundiyil, P. Poornesh, K. Ozga, B. Sahraoui, D. Guichaoua and S. Taboukhat, *et al.*, Composition engineering of spray pyrolyzed Mn-doped nickel oxide nanostructures for photonics applications in ultrafast temporal regimes, *Ceram. Int.*, 2025, **51**(27), 52583–52598, DOI: 10.1016/j.ceramint.2025.09.015.
15 M. Najafi and H. Eshghi, The effect of Cu-doping on physical properties of nanostructured NiO thin films prepared by spray pyrolysis technique, *Sci. Iran.*, 2015, **22**, 1317–1321.
16 R. Balakarthikeyan, A. Santhanam, R. Anandhi, S. Vinoth and A. M. Al-baradi, Fabrication of nanostructured NiO and NiO: Cu thin films for high-performance ultraviolet photodetector, *Opt. Mater.*, 2021, **120**, 111387, DOI: 10.1016/j.optmat.2021.111387.
17 D. Naveena, T. Logu, K. Sethuraman and A. C. Bose, Significant enhancement of photo-physicochemical properties of Yb doped copper oxide thin films for efficient solid-state solar cell, *J. Alloys Compd.*, 2019, **795**, 187–196.
18 K. N. Patel, M. P. Deshpande, K. Chauhan, P. Rajput, V. P. Gujarati and S. Pandya, *et al.*, Effect of Mn doping concentration on structural, vibrational and magnetic properties of NiO nanoparticles, *Adv. Powder Technol.*, 2018, **29**, 2394–2403, DOI: 10.1016/j.apt.2018.06.018.
19 T. Indumathi, A. H. Hirad, A. A. Alarfaj, E. Ranjith Kumar and K. Chandrasekaran, Phytoextract-mediated synthesis of Cu doped NiO nanoparticle using cullon tomentosum plant extract with efficient antibacterial and anticancer property, *Ceram. Int.*, 2023, **49**, 31829–31838, DOI: 10.1016/j.ceramint.2023.07.142.
20 T. Sen, R. Thangavel and U. Gopalakrishnan Nair, Optical and Electrical Properties of Copper Doped Nickel Oxide Thin Films by Using Sol-Gel Spin Coating Method, *Mater. Today: Proc.*, 2017, **4**, 9597–9601, DOI: 10.1016/j.matpr.2017.06.231.
21 H. Hamdy, M. S. Abdel-wahab, M. T. Tammam, M. A. K. Elfayoumi, M. Shaban and W. Z. Tawfik, Boosting UV photodetector performance with copper-doped NiO nanoflake thin films, *Phys. B*, 2025, **707**, 417196, DOI: 10.1016/j.physb.2025.417196.
22 M. N. Siddique and P. Tripathi, Lattice defects formulated ferromagnetism in nonmagnetic La (III) ion doped NiO nanostructures: Role of oxygen vacancy, *J. Alloys Compd.*, 2020, **825**, 154071, DOI: 10.1016/j.jallcom.2020.154071.
23 R. Balakarthikeyan, A. Santhanam, R. Anandhi, S. Vinoth, A. M. Al-Baradi and Z. A. Alrowaili, *et al.*, Fabrication of nanostructured NiO and NiO:Cu thin films for high-performance ultraviolet photodetector, *Opt. Mater.*, 2021, **120**, 111387, DOI: 10.1016/j.optmat.2021.111387.
24 K. Kaarthik, C. Vivek and B. Balraj, Enhanced ultra violet photo detecting properties of La3+ ions doped NiO nanoparticles, *J. Photochem. Photobiol., A*, 2024, **452**, 115480, DOI: 10.1016/j.jphotochem.2024.115480.
25 W. Geng, P. Song, X. Cao and L. Duan, Bimetallic Ni/V-MOFs-derived Ni3V2O8@NiO hollow microspheres for ultrasensitive detection of triethylamine, *Appl. Surf. Sci.*, 2024, **670**, 160637. Available from: https://linkinghub.elsevier.com/retrieve/pii/S0169433224013503.
26 S. B. Patil, S. V. Desarada, A. M. Teli, S. Vallabhapurapu, J. C. Shin and S. B. Sadale, Nucleation, growth mechanism, and bifunctional electrochromic supercapacitive properties of NiO thin films, *Ceram. Int.*, 2024, **50**, 56109–56122, DOI: 10.1016/j.ceramint.2024.10.079.
27 M. A. Hefnawy, S. A. Fadlallah, R. M. El-Sherif and S. S. Medany, Synergistic effect of Cu-doped NiO for enhancing urea electrooxidation: Comparative electrochemical and DFT studies, *J. Alloys Compd.*, 2022, **896**, 162857, DOI: 10.1016/j.jallcom.2021.162857.
28 G. Manibalan, G. Murugadoss, P. Kuppusami, N. Kandhasamy and M. Rajesh Kumar, Synthesis of heterogeneous NiO nanoparticles for high-performance electrochemical

supercapacitor application, *J. Mater. Sci.: Mater. Electron.*, 2021, **32**, 5945–5954, DOI: 10.1007/s10854-021-05315-9.

29 Y. Xie, Y. Guo, Y. Guo, L. Wang, W. Zhan and Y. Wang, *et al.*, A highly effective Ni-modified MnO: X catalyst for total oxidation of propane: The promotional role of nickel oxide, *RSC Adv.*, 2016, **6**, 50228–50237.

30 Y. Gao, J. Xu, S. Shi, H. Dong, Y. Cheng and C. Wei, *et al.*, TiO 2 Nanorod Arrays Based Self-Powered UV Photodetector: Heterojunction with NiO Nanoflakes and Enhanced UV Photoresponse, *ACS Appl. Mater. Interfaces*, 2018, **10**, 11269–11279. Available from: https://pubs.acs.org/doi/10.1021/acsami.7b18815.

31 S. Dolai, R. Dey, S. Das, S. Hussain, R. Bhar and A. K. Pal, Cupric oxide (CuO) thin films prepared by reactive d.c. magnetron sputtering technique for photovoltaic application, *J. Alloys Compd.*, 2017, **724**, 456–464, DOI: 10.1016/j.jallcom.2017.07.061.

32 S. C. Chen, T. Y. Kuo, Y. C. Lin and H. C. Lin, Preparation and properties of p-type transparent conductive Cu-doped NiO films, *Thin Solid Films*, 2011, 4944–4947, DOI: 10.1016/j.tsf.2011.01.058.

33 M. Nesa, M. Sharmin and A. H. Bhuiyan, Role of Zn dopants on the surface morphology, chemical structure and DC electrical transport properties of nanostructured p-type CuO thin films, *Mater. Sci. Semicond. Process.*, 2021, **122**, 105479, DOI: 10.1016/j.mssp.2020.105479.

34 V. Ganesh, M. Shkir, M. Anis and S. AlFaify, Structural, morphological and opto-nonlinear studies of Cu:NiO: Glass thin films facilely designed by spin coater for electro-optics, *Mater. Res. Express*, 2019, **6**(8), 086439, DOI: 10.1088/2053-1591/ab2090.

35 I. Jellal, K. Nouneh, J. Jedryka, D. Chaumont and J. Naja, Non-linear optical study of hierarchical 3D Al doped ZnO nanosheet arrays deposited by successive ionic adsorption and reaction method, *Opt. Laser Technol.*, 2020, **130**, 106348, DOI: 10.1016/j.optlastec.2020.106348.

36 G. Essalah, H. Guermazi, S. Guermazi, J. Jedryka, K. Ozga and A. Antony, *et al.*, Enhanced sunlight photo-catalytic performances of ZnO/ZnNb2O6/Nb2O5 composites for organic pollutant degradation, *Opt. Mater.*, 2023, **138**, 113637.

37 X. H. Wang, D. P. West, N. B. McKeown and T. A. King, Determining the cubic susceptibility (3) of films or glasses by the Maker fringe method: a representative study of spin-coated films of copper phthalocyanine derivation, *J. Opt. Soc. Am. B*, 1998, **15**, 1895.

38 A. Szukalska, K. Cyprych, H. El Karout, K. Waszkowska, E. Chrzumnicka and B. Sahraoui, *et al.*, A systematic evaluation of Random Lasing, Third Harmonic Generation, and quantum chemical calculations in multifunctional perylene derivatives, *J. Alloys Compd.*, 2024, **1009**, 176917, DOI: 10.1016/j.jallcom.2024.176917.

39 K. Kubodera and H. Kobayashi, Determination of Third-Order Nonlinear Optical Susceptibilities for Organic Materials by Third-Harmonic Generation, *Mol. Cryst. Liq. Cryst. Incorporating Nonlinear Opt.*, 1990, **182**, 103–113. Available from: https://www.tandfonline.com/doi/abs/10.1080/00268949008047792.

40 K. Waszkowska, V. Smokal, M. Karakaya, A. Karakas, A. V. Kityk and A. Migalska-Zalas, *et al.*, Tailoring Nonlinear Optical Response: Impact of Substituents in Thiazole-Azo Polymers, *Spectrochim. Acta, Part A*, 2025, **343**, 126495, DOI: 10.1016/j.saa.2025.126495.

41 P. Płóciennik, D. Guichaoua, A. Zawadzka, A. Korcala, J. Strzelecki and P. Trzaska, *et al.*, Optical properties of MgO thin films grown by laser ablation technique, *Opt. Quantum Electron.*, 2016, **48**, 1–12.

42 T. Chtouki, L. Soumahoro, B. Kulyk, H. Erguig, B. Elidrissi and B. Sahraoui, Spin-coated Tin-doped NiO thin films for third order nonlinear optical applications, *Optik*, 2017, **136**, 237–243, DOI: 10.1016/j.ijleo.2017.01.110.

43 T. Chtouki, L. Soumahoro, B. Kulyk, H. Bougharraf, B. Kabouchi and H. Erguig, *et al.*, Comparison of structural, morphological, linear and nonlinear optical properties of NiO thin films elaborated by Spin-Coating and Spray Pyrolysis, *Optik*, 2017, **128**, 8–13, DOI: 10.1016/j.ijleo.2016.10.007.

44 S. Abed, K. Waszkowska, H. Djaaboube, A. Bouabellou, S. Taboukhat and B. Sahraoui, *et al.*, Zinc doping-induced modulation of optical and nonlinear optical properties in MgO thin films deposited by dip coating, *Opt. Quantum Electron.*, 2025, **57**, 275, DOI: 10.1007/s11082-025-08187-z.

45 T. Chtouki, S. Taboukhat, H. Kavak, A. Zawadzka, H. Erguig and B. Elidrissi, *et al.*, Characterization and third harmonic generation calculations of undoped and doped spin-coated multilayered CuO thin films, *J. Phys. Chem. Solids*, 2019, **124**, 60–66, DOI: 10.1016/j.jpcs.2018.08.035.

46 M. Sheik-Bahae, A. A. Said, T. H. Wei, D. J. Hagan and E. W. Van Stryland, Sensitive Measurement of Optical Nonlinearities Using a Single Beam, *IEEE J. Quantum Electron.*, 1990, **26**, 760–769.

47 A. D. Rao, R. Bairy, Preethika, S. D. Kulkarni and N. Gummagol, Laser-induced non-linear optical properties of transparent conducting Sn1-xNixO2 thin films prepared by spray pyrolysis for optoelectronic device application, *Appl. Nanosci.*, 2025, **15**, 22, DOI: 10.1007/s13204-025-03098-7.

48 N. Priyadarshani, G. Vinitha and T. C. Sabari Girisun, Third order nonlinear optical properties of monoclinic and orthorhombic CuNb2O6 under CW laser illumination, *Opt. Laser Technol.*, 2018, **108**, 287–294, DOI: 10.1016/j.optlastec.2018.06.040.

49 V. Ganesh, L. Haritha, M. Anis, M. Shkir, I. S. Yahia and A. Singh, *et al.*, Structural, morphological, optical and third order nonlinear optical response of spin-coated NiO thin films: An effect of N doping, *Solid State Sci.*, 2018, **86**, 98–106, DOI: 10.1016/j.solidstatesciences.2018.10.009.

50 V. Ganesh, M. Shkir, M. Anis and S. AlFaify, Structural, morphological and opto-nonlinear studies of Cu:NiO: glass thin films facilely designed by spin coater for electro-optics, *Mater. Res. Express*, 2019, **6**, 086439. Available from: https://iopscience.iop.org/article/10.1088/2053-1591/ab2090.

51 F. Asaldoust, K. Mabhouti, A. Jafari and M. Taleb-Abbasi, Study of Z-scan technique, dispersion energy, and Wemple–DiDomenico model on Cu, Cr and Fe doped NiO nanopowder for the determination of nonlinear and linear optical characteristics, *Sci. Rep.*, 2025, **15**, 9963. Available from: **https://www.nature.com/articles/s41598-025-94079-x**.

52 P. S. Menon, J. Kunjumon, M. Bansal, S. S. Nair, C. Beryl and G. Vinitha, *et al.*, Role of surface defects in the third order nonlinear optical properties of pristine NiO and Cr doped NiO nanostructures, *Ceram. Int.*, 2023, **49**, 5815–5827, DOI: **10.1016/j.ceramint.2022.10.301**.

53 J. Mathai, A. K. Jose, M. P. Anjana, P. A. Aleena, J. Kunjumon and R. Ittyachan, *et al.*, Substantial effect of Cr doping on the third-order nonlinear optical properties of ZnO nanostructures, *Opt. Mater.*, 2023, **142**, 114128, DOI: **10.1016/j.optmat.2023.114128**.

54 Y. S. Tamgadge, V. G. Pahurkar, S. S. Talwatkar, A. L. Sunatkari and G. G. Muley, Thermally stimulated third-order optical nonlinearity in Cd-doped CuO–PVA thin films under cw laser illumination, *Appl. Phys. B: Lasers Opt.*, 2015, **120**, 373–381.

55 P. S. Menon, J. Kunjumon, A. K. Jose, P. A. Aleena, M. Bansal and G. Vinitha, *et al.*, Structural, Third Order Nonlinear and magnetic properties of pristine and Ni-doped CuO nanoparticles: Diluted magnetic semiconductors, *Colloids Surf., A*, 2022, **650**, 129582, DOI: **10.1016/j.colsurfa.2022.129582**.

56 M. Makkar, M. Barala, K. Nanda, N. Gummagol and D. Mohan, Optical nonlinearity in CuO thin films for the generation of hollow Gaussian beam, *Phys. Scr.*, 2025, **100**, 065958, DOI: **10.1088/1402-4896/add576**.

57 P. Divya, B. Vijayakumar, N. A. L. Flower, R. A. Sujatha, G. Vinitha and K. M. Rahulan, Defect state enhanced third order thermo-optic nonlinearity in Bi3+ doped MnWO4 nanostructures, *Appl. Phys. A: Mater. Sci. Process.*, 2025, **131**, 1–13.

58 A. S. Alattar, M. Nadafan, Z. Dehghani and M. Khashehchi, Influence of d-d transition electrons and thickness variations on the excited-state optical properties: Nonlinear optical characterization of Cr2O3 thin film, *J. Lumin.*, 2025, **277**, 120916, DOI: **10.1016/j.jlumin.2024.120916**.

59 R. Pooja Shaji, J. Kunjumon, P. A. Aleena, A. K. Jose, S. S. Shaiju and S. S. Nair, *et al.*, Influence of cobalt doping on the structural and third order nonlinear optical properties of MgO nanostructures, *Mater. Sci. Eng., B*, 2025, **321**, 118507, DOI: **10.1016/j.mseb.2025.118507**.

